Title

Molecular Mechanisms of the Membrane Sculpting ESCRT Pathway

Author

Remec Pavlin, Mark

Publication Date

2020

Peer reviewed|Thesis/dissertation

Molecular Mechanisms of the Membrane Sculpting ESCRT Pathway

By

Mark Remec Pavlin

A dissertation submitted in partial satisfaction of the

requirements for the degree of

Doctor of Philosophy

in

Biophysics

in the

Graduate Division

Of the

University of California, Berkeley

Committee in charge:

Professor James Hurley, Chair
Professor Daniel Fletcher
Professor Karen Davies
Professor Niren Murthy

Summer 2020

Abstract

Molecular Mechanisms of the Membrane Sculpting ESCRT Pathway

By

Mark Remec Pavlin

Doctor of Philosophy in Biophysics

University of California, Berkeley

Professor James Hurley, Chair

The Endosomal Sorting Complex Required for Transport (ESCRT) is an ancient, complex machinery that remodels and scissions cellular membranes. Uniquely, the ESCRTs remodel and scission membranes in a reverse topology – away from the cytosol. Since their discovery the ESCRTs have been identified in a large number of cellular processes, but detailed mechanistic understanding has proven difficult. As a system of over 20 components that rapidly and dynamically rearrange themselves to constrict and scission membranes, the ESCRTs prove a difficult machinery that will require high-quality reconstitutions to study.

In Chapter 1 I provide an introduction to the ESCRTs and describe recent advances toward achieving a consensus on the mechanism of ESCRT-mediated membrane remodeling and scission. In Chapter 2 I discuss the first reconstitution of ESCRT-mediated membrane scission, combining microscopy, microfluidics, and optical trapping to achieve this goal. In Chapter 3 I describe a novel function of the ESCRTs, finding that CHMP1B, IST1, and Spastin are capable of normal-topology membrane scission. Finally, in Chapter 4 I provide an outlook on the remaining challenges in the field, and the approaches that will be crucial for tackling them.

Dedication

To my ever loving, ever supportive parents

Table of Contents:

Acknowledgements

Berkeley is an incredible community of not only brilliant scientists, but kind and generous people. I am deeply grateful for all of the wonderful mentors, collaborators, and coworkers I have been fortunate enough to work with.

Chapter 1

The ESCRTs: Converging on Mechanism

Abstract

The endosomal sorting complexes required for transport (ESCRT) I, -II and -III and their associated factors are a collection of approximately 20 proteins in yeast and approximately 30 in mammals, responsible for severing membrane necks in processes that range from multivesicular body formation, HIV release, and cytokinesis to plasma and lysosomal membrane repair. ESCRTs are best known for 'reverse topology' membrane scission, where they act on the inner surface of membrane necks, often when membranes are budded away from the cytosol. These events are driven by membrane-associated assemblies of dozens to hundreds of ESCRT molecules. ESCRT-III proteins form filaments with a variety of geometries, and now ESCRT-I has been shown to form helical structures as well. The complex nature of the system and the unusual topology of its action have made progress challenging and led to controversies with regard to its underlying mechanism. This Review will focus on recent advances obtained by structural, *in vitro* reconstitution and *in silico* mechanistic studies, and places them in biological context. The field is converging towards a consensus on the broad outlines of a mechanism that is driven by progressive ATP-dependent treadmilling exchange of ESCRT subunits, as well as compositional change and geometric transitions in ESCRT filaments.

Introduction

The endosomal sorting complexes required for transport (ESCRT) are an ancient, multi-component membrane remodeling complex capable of bringing membrane necks to abscission in a reverse topology manner. In other words, the ESCRTs can sever membranes that are budding away from the cytoplasm rather than toward the cytoplasm as in endocytosis (Hurley, 2015; Vietri et al., 2020). The ESCRTs originated in a subset of the Archaea, where they are involved in cytokinetic membrane constriction and abscission (Samson et al., 2008; Risa et al., 2019). In eukaryotes, the ESCRTs are involved in an enormous number of cellular processes (Hurley, 2015; Vietri et al., 2020). Most famously, the ESCRTs are essential for multivesicular body biogenesis (Babst et al., 2011), HIV egress (Sundquist and Kräusslich, 2012; Hurley and Cada, 2018), exosome production (Colombo et al., 2013), cytokinesis (Carlton and Martin-Serrano, 2007), as well as nuclear envelope surveillance and/or resealing (Webster et al., 2014; Olmos et al., 2015; Vietri et al., 2015; Raab et al., 2016). More recently identified functions include plasma-membrane repair (Jimenez et al., 2014; Scheffer et al., 2014), autophagosome closure (Takahashi et al., 2018), and lysosome repair (Skowyra et al., 2018; Radulovic et al., 2018). In addition to these reverse-topology scission functions, ESCRTs can also carry out normal topology scission (McCullough et al., 2015). The ESCRTs therefore comprise a versatile membrane remodeling machinery with a vast array of functions in eukaryotes, and their mechanism of action has naturally attracted a great deal of investigative effort.

The ESCRTs constitute a system of around 20 proteins in yeast and over 30 in mammals, summarized in Table 1. They consist of the complexes ESCRT-0, ESCRT-I, ESCRT-II, and ESCRT-III, the AAA+ ATPase Vps4, and associated proteins that include ALG-2 Interacting Protein X (ALIX)/ BCK1-like resistance to osmotic shock protein 1 (Bro1), His domain-containing protein tyrosine phosphatase (HD-PTP) and others. Other reviews have extensively described the properties of the individual ESCRT proteins and sub-complexes (Schöneberg et al., 2016; McCullough et al., 2018), so we will here present only a brief overview. ESCRT-0 proteins are best characterized in multi-vesicular body (MVB) biogenesis. ESCRT-0 is an endosomal clathrin adaptor that initiates ESCRT recruitment during MVB biogenesis, but has no direct role in membrane remodeling. The ESCRT-I complex is shaped as a long stalk with a head that recruits the ESCRT-II complex (Kostelansky et al., 2007; Boura et al., 2012). The ESCRT-II complex has a Y-shaped architecture (Hierro et al., 2004, Teo et al., 2004) with two binding sites for Vps20 (CHMP6 in humans) (Im and Hurley, 2008), the most upstream of the ESCRT-III proteins the first ESCRT-III recruited in the pathway.

Complex	Yeast	Human
ESCRT-I	Vps23	TSG101
	Vps28	Vps28
	Vps37	Vps37A/B/C/D
	Mvb12	MVB12A/B; UBAP1
ESCRT-II	Vps22	EAP30
	Vps36	EAP45
	Vps25	EAP20
ESCRT-III	Vps20	CHMP6
	Snf7	CHMP4
	Vps24	CHMP3
	Vps2	CHMP2
	Did2	CHMP1
	Ist1	IST1
	Cmp7p	CHMP7
	Vps60	CHMP5
AAA+ ATPase	Vps4	VPS4A/B
	Spastin	SPASTIN
Adaptors	Bro1	ALIX

Table 1.1: A summary of the ESCRT complexes and their constituent subunits

ESCRT-III proteins are highly basic proteins that bind readily to negatively charged membranes and are capable of polymerizing into large assemblies of various architectures and curvatures, thought to drive membrane constriction (Lee et al., 2015; McCullough et al., 2018). In addition to Vps20/CHMP6, mechanistic research into membrane severing has focused mainly on Snf7/CHMP4, Vps24/CHMP3, Vps2/CHMP2, IST1, and Did2/CHMP1B. Of the two other subunits, Cmp7p/CHMP7 exerts specialized functions in nuclear surveillance and repair (Olmos et al, 2016), and Vps60/CHMP5 remains poorly characterized. Structural work revealed the ESCRT-IIIs to be small, helical proteins (Muziol et al., 2006) that exist in an autoinhibited, closed state in the cytosol (Zamborlini et al., 2006; Shim et al., 2007; Bajorek et al., 2009); however, some, including Snf7 and CHMP1B, adopt an open, extended conformation on membranes (McCullough et al., 2015; Tang et al., 2015; McMillan et al., 2016). Finally, the AAA+ ATPase Vps4 (Babst et al., 1998) is recruited membranes to translocate and unfold (Yang et al., 2015) ESCRT-III components; this is mediated through a Microtubule Interacting and Trafficking (MIT)-MIM-interacting motif (MIM) interaction with various ESCRT-III proteins (Stuchell-Brereton et al., 2007; Obita et al., 2007; Yang et al., 2008).

Foundational studies of overexpressed (Hanson et al., 2008) and reconstituted (Lata et al., 2008) ESCRT-III complexes showed that ESCRTs were capable of forming helical tubes (Hanson et al., 2008; Lata et al., 2008) and spirals (Hanson et al., 2008; Cashikar et al., 2014) on membranes. An influential early model of ESCRT-III function stemmed from the observation that the ESCRT-III components CHMP2 and CHMP3 can assemble into tubes that end in a dome cap (Fabrikant et al., 2009; Effantin et al., 2013) and which can be disassembled by VPS4 (Lata et al., 2008). This proposed model suggested that the CHMP2-CHMP3 heteropolymer templates the membrane from the inside until the domed cap and protein-lipid adhesion energy bring the two leaflets close enough to allow fission in conjunction with VPS4 activity.

ESCRTs can also carry out membrane scission in normal topology, in other words, acting from the positively curved outer surface of membrane tubes. In cells depleted of the ESCRT-III subunit IST1, recycling tubular endosomes cannot be scissioned, which impaired lysosomal trafficking (Allison et al., 2017; Allison et al., 2019). The AAA+ ATPase spastin, which is best known as a microtubule-severing enzyme but also interacts strongly with IST1 and CHMP1B, another ESCRT-III subunit, is involved in normal topology scission by ESCRTs. IST1, CHMP1B, and spastin are important for trafficking of lipids between lipid droplets and peroxisomes in a yet unclear mechanism (Chang et al., 2019). In addition, ESCRTs have been shown to be also essential for the release of new peroxisomes from the endoplasmic reticulum (ER) (Mast et al., 2018), another likely function that involved normal-topology scission.

In this Review, we will summarize recent data and insights on ESCRT-mediated mechanisms, with an emphasis on *in vitro* and *in silico* studies. We will describe major advances that have been afforded by advances in techniques, such as cryo-EM that have made it possible to characterize the various large-scale assemblies formed by ESCRT-III subunits, synthetic membrane biochemistry to reconstitute ESCRT scission using minimal components and simplified membrane compositions, as well as the use of optical tweezers in reconstituted systems. We will conclude with an attempt to converge the available data into what we consider a most-likely mechanistic model, as well as outline crucial further experiments that might yield important new insights in the future.

Bulk membrane biochemical studies

Early *in vitro* studies reported that yeast ESCRT-III proteins could bud and sever Intraumenal Vesicles (ILVs) using giant unilamellar vesicles (GUVs) as substrates (Wollert et al., 2009; Wollert and Hurley, 2010). This reaction corresponds to the role of ESCRTs in MVB biogenesis, where ESCRTs are responsible both for creating membrane buds and severing them into the lumen. This process is distinct from most other ESCRT functions in the cell, where the membrane neck is created by other machineries. In the *in vitro* studies, GUVs with a negative charge density that is sufficient to recruit ESCRTs were incubated with various ESCRT components, either added simultaneously or sequentially, and ILVs were thereafter observed in the lumen of the GUV (Wollert et al., 2009). By adding a membrane-impermeable dye to the GUV mix prior to initiating the ESCRT reaction, we could show that ILV formation was dependent on the appropriate mixture of ESCRTs including Vps20, Snf7, Vps24, and Vps2 (Wollert et al., 2009). The ATPase Vps4 was unnecessary for the initial round of budding and scission events under these conditions, but it did contribute to recycling of ESCRTs for additional budding (Wollert et al., 2009). These findings were contradicted, however, by a series of subsequent cell-imaging studies that consistently found that Vps4 is recruited to sites of ESCRT action prior to scission (Baumgärtel et al., 2011; Jouvenet et al., 2011; Bleck et al., 2014; Adell et al., 2017; Mierzwa et al., 2017; Johnson et al., 2018).

Recent studies have reproduced and extended these observations. A lipidated, chimeric yeast Snf7-Vps2 construct was shown to be capable of generating ILVs in GUVs, although complete scission of the ILVs into the lumen of the GUV with such a minimal ESCRT functionality was inefficient (Marklew et al., 2018). Similar findings were reported in a study of *Entamoeba histolytica* ESCRT-III proteins on GUVs (Avalos-Padilla et al., 2018). In addition, yeast ESCRT-III proteins were used to probe the effects of membrane tension and protein stoichiometry on ILV formation in GUVs and found that tension, but not the relative concentrations of each subunit, was a key factor determining successful ILV formation (Booth et al., 2019). These findings are consistent with *in vivo* observations that a decrease in tension on endosomes triggers ESCRT recruitment and function on the membrane (Mercier et al., 2019). These results support an intriguing feedback model: low membrane tension favors ESCRT-mediated formation of intraluminal vesicles, which causes a loss of membrane area with a consequent tension increase in the GUV or endosome, and this tension increase then inhibits further ESCRT function (Booth et al., 2019). Indeed, one confounding factor of using GUVs as templates to understand ESCRT function on cellular membranes may be their lack of rigidity. Since GUVs typically have lower bending rigidities and lower tension values than cellular membranes (Dimova et al., 2006), it is possible that the apparent Vps4 independence of scission in GUVs observed previously could be related to the deformability of GUVs. Collectively, although the GUV system ultimately proved to be too permissive to completely reflect the biology, these experiments nevertheless established the important point that the core ESCRT-III proteins Snf7, Vps24, and Vps2 comprise, in principle, a minimal machinery for membrane scission.

Membrane nanotube experiments

Membrane nanotubes that are pulled from GUVs provided a more controlled setting for reconstitution and real-time imaging of single ESCRT-mediated scission events. In this modality, streptavidin-coated beads held in an optical trap can be used to pull membrane tubes of tens of nm in diameter from GUVs under conditions of controlled membrane tension and force (Sorre et al., 2009; Prevost et al., 2017). Indeed, recent experiments from our lab and others have used such a setup to probe ESCRT function on small membrane tubes pulled from GUVs by dielectric beads held in an optical trap (Schöneberg et al., 2018; Pfitzner et al., 2019). This pulled nanotube comprises a membrane neck Gaussian curvature geometry similar to the physiological substrates of the ESCRTs. In the first study of this type (Schöneberg et al., 2018) Snf7, Vps24, Vps2 Vps4 and caged ATP were encapsulated within GUVs using poly-vinyl alcohol (PVA) swelling of lipid films (Fig 1.1 A). Prior to ATP uncaging by UV-illumination, ESCRT proteins including Vps4 were observed exclusively in the lumen of the GUV. An alternative technique, depicted in Fig 1.1 B, uses laser-mediated fusion of a protein-containing, neutrally-charged GUV with an empty, negatively charged GUV to prevent the proteins from binding the negatively charged lipids prematurely (De Franceschi et al., 2019). The GUVs were aspirated onto a micropipette to control membrane tension, before a tube was pulled from the GUV. After ATP uncaging, the ESCRT-III proteins and Vps4 began to accumulate in puncta along the length of the tube, and a progressively increasing force on the trapped bead was measured over timescales of minutes to tens of minutes. Furthermore, Snf7 and Vps4 were seen to steadily co-accumulate at up to a few hundred subunits each, which is roughly consistent with quantitation from live-cell imaging (Adell et al., 2017). The increase in force was concurrent with an increase in the fluorescence intensity of the puncta and a decrease in the tube radius to a radius below 10 nanometers and culminated in scission of the tube from the GUV, shown in Fig 1.1 C (Schöneberg et al., 2018).

A subsequent study reproduced these results and extended them by including the additional components Did2 and Ist1, demonstrating that, as expected, scission is more efficient when more of the ESCRT components are included (Pfitzner et al., 2019). In order to avoid encapsulating ESCRTs within GUVs, this study used tubes that were pushed into the lumen of the GUV with the ESCRTs on their outside (Fig 1.1 D), rather than pulling a tube out of the GUV with ESCRTs inside as described above. The authors further concluded that the precise composition of the ESCRT-III assembly is crucial for regulating deformation of the tube and its scission, with particularly important roles for Did2 and Ist1. Did2 appears to promote buckling and tubulation of ESCRT assemblies, while Ist1 facilitates constriction, but blocks scission. Based on these findings, the authors suggest that remodeling of the ESCRT-III filament by Did2 causes initial deformation, after which Ist1 induces the final constriction. The subsequent removal of Ist1 from the filament then allows Vps4-mediated scission to occur (Pfitzner et al., 2019). However, the endosomal sorting phenotypes of *ist1Δ* and *did2Δ* yeast are quite mild (Dimaano et al., 2008; Rue et al., 2007), and it therefore remains to be reconciled how these *in vitro* findings relate to the biological function *in vivo*.

ESCRT and membrane mechanics

In silico simulations and modeling, are becoming increasingly important in understanding key steps in mechanical events at the nanoscale such as ESCRT-mediated scission, which are intractable to experimental observation. The earliest model of ESCRT scission to be analyzed in detail was a mathematical calculation investigating whether an adhesive protein dome could sufficiently deform a membrane to scission. (Fabrikant et al., 2009). This calculation was subsequently found to overestimate the energy available from adhesion of the putative ESCRT dome to the membrane (Agudo-Canalejo and Lipowsky, 2018). The ability of ESCRTs to undergo buckling transitions from flat spirals to helical tubes and so deform membranes was implied from cellular EM studies (Hanson et al., 2008), analyzed computationally (Lenz et al., 2009) and observed experimentally (Chiaruttini et al., 2015), raising the possibility that the sudden buckling of a helical spiral in the neck of a membrane to a flat spiral could plausibly pull the membrane Using a continuum model of the forces imparted by polymerizing proteins on an elastic membrane at the neck of a pre-formed vesicle, cone-like assemblies of adhesive proteins were shown to both require less energy to constrict the neck and to be capable of imparting greater forces for constriction than dome-like assemblies (Agudo-Canalejo and Lipowsky, 2018). The energy barrier to membrane scission can be lowered further if axial symmetry is broken (Vasan et al., 2020), suggesting that the ESCRTs may constrict the membrane asymmetrically.

The most detailed mechanical analysis thus far of how ESCRT-III polymerization generates membrane deformation and constriction made use of coarse-grained molecular simulations (Harker-Kirschneck et al., 2019). Here, a coarse-grained approximation of individual ESCRT-III subunits as a triplet of beads connected by springs was applied onto a one-bead-per-lipid approximation of an initially flat lipid bilayer. In the simulation, the filaments were driven to alternately tilt and flatten. By adding a model membrane-bound cargo that is capable of interacting with ESCRT beads to the simulation, the authors showed that the combination of the cargo stabilizing the bud curvature, in competition with the tilting and flattening (i.e., buckling) of ESCRT filaments, was sufficient to progressively constrict and sever the membrane neck (Harker-Kirschneck et al., 2019). Importantly this model recapitulates the buckling observed previously (Chiaruttini et al., 2015), but with significantly fewer subunits being required, bringing this model into closer alignment with protein copy numbers measured *in vivo* (Adell et al., 2017). Taken together, these *in silico* studies are consistent with the idea that transitions in filament geometry at the membrane neck, including buckling and symmetry breaking, drive membrane scission.

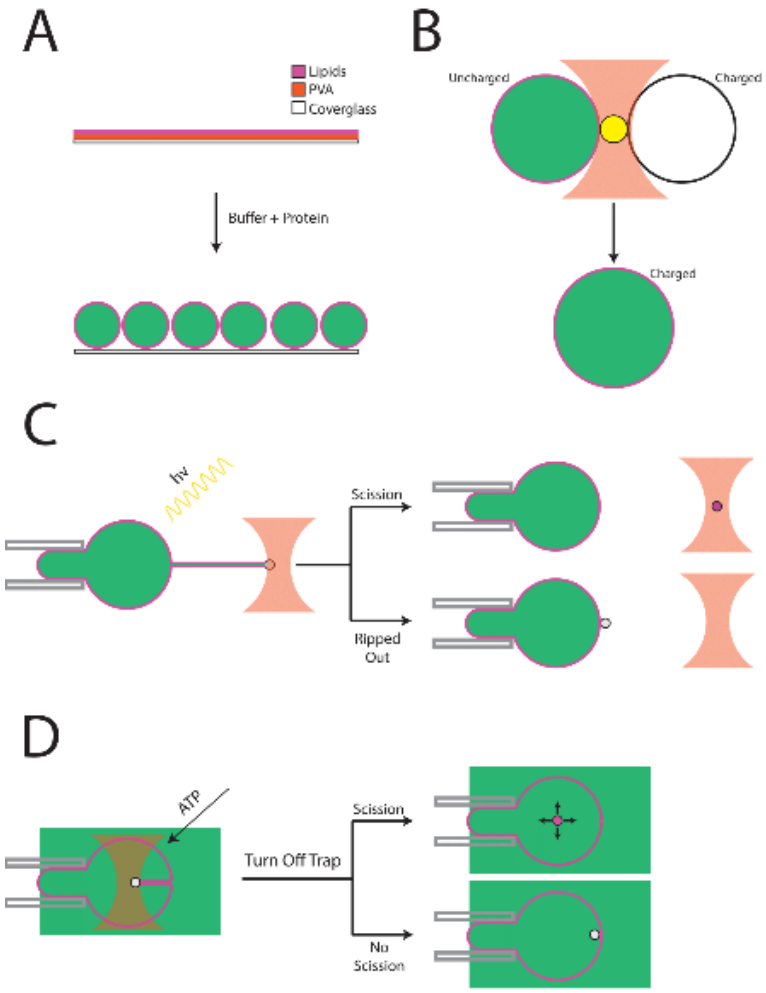

Fig 1.1: Illustration of experimental techniques. (A) Swelling Giant Unilamellar Vesicles: a thin film of poly-vinyl alcohol (PVA) helps dried lipid films swell into GUVs upon addition of buffer or protein. PVA swelling tolerates high salt concentrations, allowing for protein encapsulation. (B) A neutrally charged GUV containing proteins that bind acidic lipids is brought into contact with a gold nanoparticle and a GUV containing high negative charge. Laser irradiation of the nanoparticle induces fusion of the two vesicles. (C) After a membrane nanotube is formed, UV illumination uncages the ATP present and ESCRT activity is observed. As the force to hold the bead rises, the membrane nanotube either scissions or pulls the bead out of the optical trap. (D) A membrane nanotube is pulled into the lumen of the GUV, with the ESCRT proteins outside. ESCRT proteins nucleate inside the membrane nanotube, and the addition of ATP triggers ESCRT activity. Scission is assayed by releasing the bead and observing whether it undergoes free diffusion, signifying scission, or a rapid pullback to the membrane, indicating that the membrane nanotube was still attached.

Compositional control of scission

ESCRTs act at membrane necks that have negative Gaussian curvature, yet individual ESCRT-III subunits do not prefer this geometry. Indeed, filaments of pure Snf7 and CHMP4, the most abundant structural component of ESCRT-III, form flat spirals (Shen et al., 2014; Chiaruttini et al., 2015). In addition, CHMP1B alone and in combination with either Ist1 (McCullough et al., 2015), and CHMP2 with CHMP3 (Bertin et al., 2019) preferentially bind to positively curved membranes. However, combinations of Snf7 with both Vps24 andVps2, or CHMP2 with both

CHMP3 and CHMP4, preferentially localize to bud necks (Schöneberg et al., 2018; Bertin et al., 2019). In fact, the presence of Vps2 and Vps24 radically alters the geometry of Snf7 filaments from flat spirals to three-dimensional helices (Henne et al., 2012; Bertin et al., 2019; von Filseck et al., 2019). When bound to membranes, the Snf7-Vps24-Vps2 and CHMP2-3-4 combinations deform liposomes into helical tubes that are coated with these ESCRT subunits on their exterior positively-curved surface (Bertin et al., 2019; von Filseck et al., 2019). While the link between these unusual helical tubular structures and biological ESCRT-III-mediated reactions is unclear, the dramatic remodeling events observed *in vitro* indicate that changes in ESCRT-III subunit composition profoundly alter its membrane-remodeling properties.

High-resolution structural data on CHMP1B and IST1 has revealed that these subunits act together to remodel, and presumably sever, positively-curved tubular endosomes (McCullough et al., 2015). A recent cryo-EM study has shown that CHMP1B alone forms a single-start helical coat of 28 nm diameter around lipid tubes (Nguyen et al., 2020). Addition of IST1 leads to a constriction of the coat to 18 nm diameter, constricting the lumen to a mere 4nm, which is presumably sufficient for membrane scission to take place. Constriction is accomplished by the flexing of the helical core of CHMP1B about an elbow joint between helices α3 and α4 (Nguyen et al., 2020). This work thus presents an important advance in the field as it allows us to understand normal-topology scission by CHMP1B and IST1 at the structural level. It is highly conceivable that the constriction event in reverse-topology scission will also depend on a compositional change and elbow-joint flexing. To solve this question requires cryo-EM experiments, which are likely to be more demanding because it is not obvious how to engineer constriction from within a tube in a manner that will provide a large number of well-aligned molecules for the necessary averaging. Structural details of constriction in reverse topology scission are therefore still lacking.

Membrane constriction can be triggered in an *in vitro* system by changing ESCRT-III composition such as adding a new component. In cells, a change in ESCRT-III composition is enabled by a constant flux of Vps4-mediated treadmilling, where subunits are recycled from the membrane while new subunits bind, as demonstrated by rapid FRAP of ESCRT-III during cytokinetic abscission (Mierzwa et al., 2017). In the unique case of CHMP1B and IST1, it seems likely that spastin contributes to treadmilling on the basis of spastin's close similarity to Vps4, its ability to bind tightly to these proteins (Reid et al., 2004; Yang et al., 2008), and its role in the scission of endosomal recycling tubes (Allison et al., 2013; Allison et al., 2017; Allison et al., 2019). However, this remains to be tested directly. Treadmilling presumably drives scission as well in the *in vitro* optical tweezers studies of Vps4-mediated reverse topology scission (Schöneberg et al., 2018; Pfitzer et al., 2019). While ATP-dependent subunit recycling by Vps4, and perhaps spastin, enables treadmilling, a major open question in the field is how the system achieves the necessary compositional change. It is not immediately clear what prevents futile cycling of the same subunits by Vps4. Since scission, driven ostensibly by treadmilling, has been replicated with simple *in vitro* systems, the driving force for compositional change must be intrinsic to the membrane-ESCRT-III-Vps4 system, with progressive alterations in membrane shape as the only reasonable candidate. Thus as the ESCRTs progressively constrict the membrane, the evolving shape of the membrane surface might favor the recruitment of the subset of ESCRTs which most favor further constriction, thereby driving a positive feedback loop ultimately leading to scission.

Geometry of scission

In *in vitro* systems consisting of bare lipid membranes and purified ESCRTs, formation of a bud neck is sufficient to recruit the set of core ESCRT-III proteins involved in scission (Schöeneberg et al., 2018; Bertin et al., 2019). In cells, where many proteins compete for space on membrane, ESCRT-III recruitment is tightly regulated and depends not just on membrane shape, but also on the presence of the appropriate upstream factors. With the major exception of nuclear membrane reformation, most ESCRT-mediated pathways involve the recruitment and nucleation of ESCRT-III by ESCRT-I and ESCRT-II, as well as ALIX (Schöeneberg et al, 2016). Recently, ESCRT-I has been revealed to be capable of polymerizing into helical structures containing up to ~11 subunits (Hoffman et al., 2019), fitting the ~60 nm dimension of a HIV-1 bud neck (Flower et al., 2020). We found that inhibiting this polymerization disrupts both HIV-1 egress and autophagosome closure (Flower et al., 2020), suggesting that such polymerization underlies multiple ESCRT-dependent scission pathways. Uniquely, cytokinesis, in which the ESCRTs nucleate at the outer rim of the midbody to form spirals on a 1 μm scale (Elia et al., 2011; Guizetti et al., 2011; Goliand et al., 2018), involves ESCRT assembly on a larger scale than any of the other known ESCRT-dependent processes and therefore has unique features that do not fit easily into this scheme. Coarse-grained simulations of HIV budding showed that ESCRT-I polymerization could serve as a geometrical checkpoint for viral egress by recognizing the correct neck geometry and initiating downstream ESCRT-III polymerization (Flower et al., 2020).

This new observation may hint at one of the unanswered questions in the field: the location of the bulk of the ESCRT molecules following scission. Fig. 1.2 illustrates three scenarios that follow from the premise that ESCRT-I nucleates the scission machinery from within the bud (Flower et al., 2020). The scenarios differ in whether constriction is a gradual inward tapering of the ESCRT filament (Fig. 1.2 A), whether it is strictly dependent on compositional change (Fig. 2B), or whether a buckling transition occurs (Fig. 1.2 C). The inward-tapering model gained some support from a recent EM study of VPS4 remodeling of CHMP2-CHMP3 tubes into dome-capped structures, in a transition that could bring the membrane to scission (Maity et al., 2019). Growth outward from the bud neck followed by buckling (Fig. 1.2 C) is the most consistent with membrane and filament mechanics models (Agudo-Canalejo and Lipowsky, 2018; Harker-Kirshneck et al., 2019), and is the only one of these scenarios that is compatible with both nucleation from within the bud and recycling of ESCRT-III complexes into the cytosol following scission, as depicted in Fig 1.2.

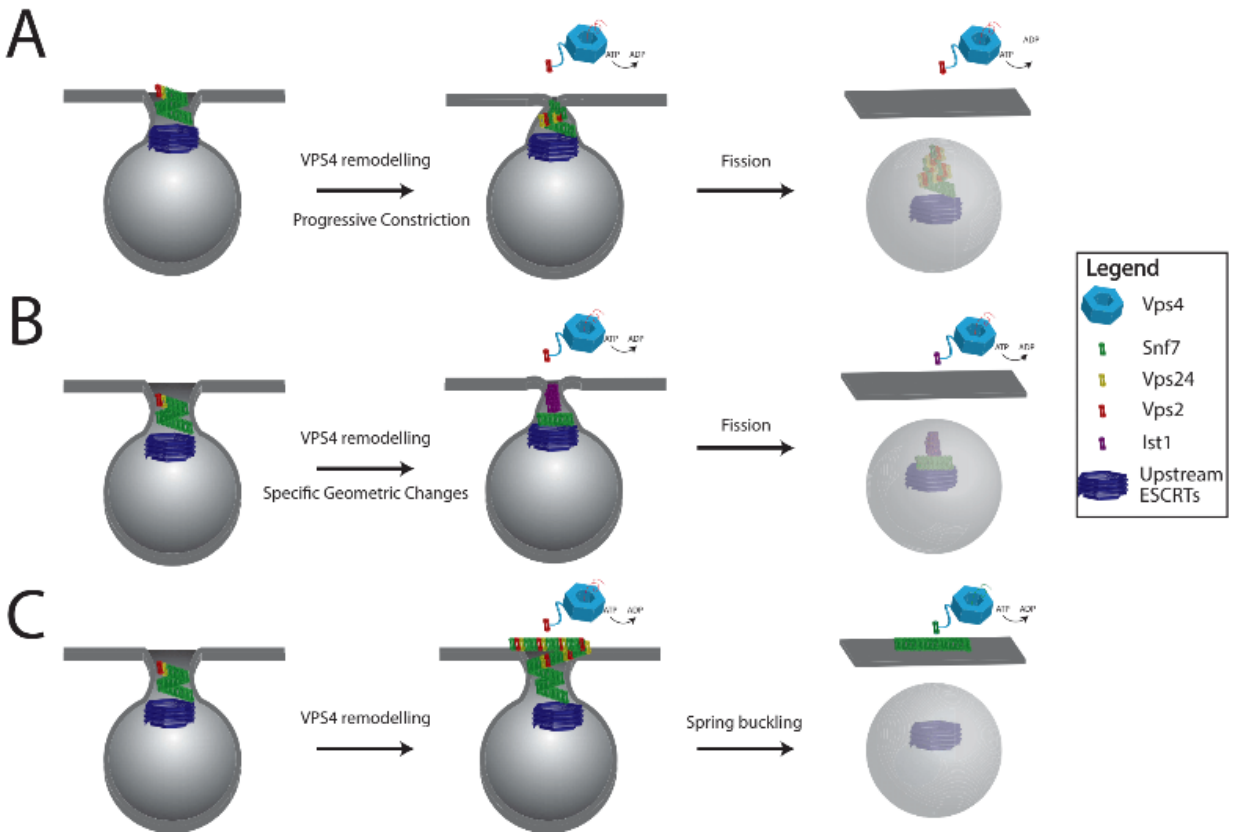

Fig 1.2: Models of ESCRT function. Upstream ESCRTs, depicted in dark blue, initially recruit the ESCRT-III subunits to the membrane neck, after which three models of constriction and scission are proposed: (A) VPS4 initiates remodeling of the ESCRT-III polymer. Compositional rearrangement driven by subunit treadmilling leads to gradual constriction and, ultimately, scission (B) Compositional rearrangement of the polymer leads to specific geometric changes that strongly constrict the membrane neck. (C) Outward spiral growth causes the polymer to suddenly buckle from a helix to a flat spiral, bringing the membrane to scission and allowing ESCRT-III to be recycled to the cytosol, in contrast to models A and B where presumably the bulk of the ESCRTs are encapsulated in the nascent vesicle.

Conclusions and perspectives

Here, we attempted to present the most recent developments in biophysical reconstitution, structural biology, and *in silico* simulations of ESCRT function, with *in vivo* data providing context and constraining the possible models. The field is now converging on a consensus mechanistic model in which a constricting spiral assembly that undergoes progressive remodeling and compositional rearrangement constricts membrane to the point of scission. That said, many key questions remain open. While it is largely accepted that the role of VPS4 is to enable compositional changes, the thermodynamic determinants of composition are still unclear. An atomic resolution description of membrane scission is only available for the two-component normal-topology scission by CHMP1B and IST1 (McCullough et al., 2015), but not yet for the more characteristic reverse-topology process. In normal-topology scission involving CHMP1B and IST1, the relative roles of VPS4 and spastin need to be clarified. Cryo-EM of scission-capable complexes in the reverse-topology process is still urgently needed to fully understand the ESCRT mechanism. Time-resolved studies with sufficient spatial resolution to address the

directionality of filament growth are also needed. The unique aspects of the large-scale structures formed in cytokinesis need further study. Given the surprising insight that ESCRT-I can form helical structures, unsuspected until recently, it will be important to determine how ESCRT-II and ALIX fit into the picture and how the upstream assemblies are regulated.

Molecular and cell biology textbooks generally portray membrane scission by the ESCRTs as a black box. The picture has become clear enough, and there is enough agreement in the field, that it is now reasonable to depict ESCRT action in the textbooks in the form of a consensus version of the models shown in Fig. 2. Those in the ESCRT field should be proud of the recent progress and optimistic that answers to the remaining questions will be forthcoming in the next few years.

References

Adell, M. A. Y., Migliano, S. M., Upadhyayula, S., Bykov, Y. S., Sprenger, S., Pakdel, M., Vogel, G. F., Jih, G., Skillern, W., Behrouzi, R., et al. (2017). Recruitment dynamics of ESCRT-III and Vps4 to endosomes and implications for reverse membrane budding. *Elife* **6**, e31652.

Agudo-Canalejo, J. and Lipowsky, R. (2018). Domes and cones: Adhesion-induced fission of membranes by ESCRT proteins. *PLOS Comput. Biol.* **14**, e1006422.

Allison, R., Edgar, J. R., Pearson, G., Rizo, T., Newton, T., Günther, S., Berner, F., Hague, J., Connell, J. W., Winkler, J., et al. (2017). Defects in ER–endosome contacts impact lysosome function in hereditary spastic paraplegia. *J. Cell Biol.* **216**, 1337–1355.

Allison, R., Edgar, J. R. and Reid, E. (2019). Spastin MIT Domain Disease-Associated Mutations Disrupt Lysosomal Function . *Front. Neurosci.* **13**, 1179.

Allison, R., Lumb, J. H., Fassier, C., Connell, J. W., Ten Martin, D., Seaman, M. N. J., Hazan, J. and Reid, E. (2013). An ESCRT–spastin interaction promotes fission of recycling tubules from the endosome. *J. Cell Biol.* **202**, 527–543.

Avalos-Padilla, Y., Knorr, R. L., Javier-Reyna, R., García-Rivera, G., Lipowsky, R., Dimova, R. and Orozco, E. (2018). The Conserved ESCRT-III Machinery Participates in the Phagocytosis of Entamoeba histolytica. *Front. Cell. Infect. Microbiol.* **8**, 53.

Babst, M. (2011). MVB vesicle formation: ESCRT-dependent, ESCRT-independent and everything in between. *Curr. Opin. Cell Biol.* **23**, 452–457.

Babst, M., Wendland, B., Estepa, E. J. and Emr, S. D. (1998). The Vps4p AAA ATPase regulates membrane association of a Vps protein complex required for normal endosome function. *EMBO J.* **17**, 2982–2993.

Bajorek, M., Morita, E., Skalicky, J. J., Morham, S. G., Babst, M. and Sundquist, W. I. (2009). Biochemical Analyses of Human IST1 and Its Function in Cytokinesis. *Mol. Biol. Cell* **20**, 1360–1373.

Baumgärtel, V., Ivanchenko, S., Dupont, A., Sergeev, M., Wiseman, P. W., Kräusslich, H.-G., Bräuchle, C., Müller, B. and Lamb, D. C. (2011). Live-cell visualization of dynamics of HIV budding site interactions with an ESCRT component. *Nat. Cell Biol.* **13**, 469–474.

Bertin, A., de Franceschi, N., de la Mora, E., Maity, S., Miguet, N., di Cicco, A., Roos, W., Mangenot, S., Weissenhorn, W. and Bassereau, P. (2019). Human ESCRT-III Polymers Assemble on Positively Curved Membranes and Induce Helical Membrane Tube Formation. *bioRxiv* 847319.

Bleck, M., Itano, M. S., Johnson, D. S., Thomas, V. K., North, A. J., Bieniasz, P. D. and Simon, S. M. (2014). Temporal and spatial organization of ESCRT protein recruitment during HIV-1 budding. *Proc. Natl. Acad. Sci. U. S. A.* **111**, 12211–6.

Booth, A., Marklew, C. J., Ciani, B. and Beales, P. A. (2019). In Vitro Membrane Remodeling by ESCRT is Regulated by Negative Feedback from Membrane Tension. *iScience* **15**, 173–184.

Boura, E., Różycki, B., Chung, H. S., Herrick, D. Z., Canagarajah, B., Cafiso, D. S., Eaton, W. A., Hummer, G. and Hurley, J. H. (2012). Solution Structure of the ESCRT-I and -II Supercomplex: Implications for Membrane Budding and Scission. *Structure* **20**, 874–886.

Carlson, L.-A., Shen, Q.-T., Pavlin, M. R. and Hurley, J. H. (2015). ESCRT Filaments as Spiral Springs. *Dev. Cell* **35**, 397–398.

Carlton, J. G. and Martin-Serrano, J. (2007). Parallels Between Cytokinesis and Retroviral Budding: A Role for the ESCRT Machinery. *Science* **316**, 1908–1912.

Cashikar, A. G., Shim, S., Roth, R., Maldazys, M. R., Heuser, J. E. and Hanson, P. I. (2014). Structure of cellular ESCRT-III spirals and their relationship to HIV budding. *Elife* **3**, e02184.

Chang, C.-L., Weigel, A. V, Ioannou, M. S., Pasolli, H. A., Xu, C. S., Peale, D. R., Shtengel, G., Freeman, M., Hess, H. F., Blackstone, C., et al. (2019). Spastin tethers lipid droplets to peroxisomes and directs fatty acid trafficking through ESCRT-III. *J. Cell Biol.* **218**, 2583–2599.

Chiaruttini, N., Redondo-Morata, L., Colom, A., Humbert, F., Lenz, M., Scheuring, S. and Roux, A. (2015). Relaxation of Loaded ESCRT-III Spiral Springs Drives Membrane Deformation. *Cell* **163**, 866–879.

Colombo, M., Moita, C., van Niel, G., Kowal, J., Vigneron, J., Benaroch, P., Manel, N., Moita, L. F., Théry, C. and Raposo, G. (2013). Analysis of ESCRT functions in exosome biogenesis, composition and secretion highlights the heterogeneity of extracellular vesicles. *J. Cell Sci.* **126**, 5553–5565.

Dimaano, C., Jones, C. B., Hanono, A., Curtiss, M. and Babst, M. (2007). Ist1 Regulates Vps4 Localization and Assembly. *Mol. Biol. Cell* **19**, 465–474.

Dimova, R., Aranda, S., Bezlyepkina, N., Nikolov, V., Riske, K. A. and Lipowsky, R. (2006). A practical guide to giant vesicles. Probing the membrane nanoregime via optical microscopy. *J. Phys. Condens. Matter* **18**, S1151–S1176.

Elia, N., Sougrat, R., Spurlin, T. A., Hurley, J. H. and Lippincott-Schwartz, J. (2011). Dynamics of endosomal sorting complex required for transport (ESCRT) machinery during cytokinesis and its role in abscission. *Proc. Natl. Acad. Sci.* **108**, 4846–4851.

Effantin, G., Dordor, A., Sandrin, V., Martinelli, N., Sundquist, W. I., Schoehn, G. and Weissenhorn, W. (2013). ESCRT-III CHMP2A and CHMP3 form variable helical polymers in vitro and act synergistically during HIV-1 budding. *Cell. Microbiol.* **15**, 213–226.

Fabrikant, G., Lata, S., Riches, J. D., Briggs, J. A. G., Weissenhorn, W. and Kozlov, M. M. (2009). Computational Model of Membrane Fission Catalyzed by ESCRT-III. *PLOS Comput. Biol.* **5**, e1000575.

Flower, T. G., Takahashi, Y., Hudait, A., Rose, K., Tjahjono, N., Pak, A., Yokom, A. L., Liang, X., Wang, H.-G., Bouamr, F., et al. (2020). A helical assembly of human ESCRT-I scaffolds reverse-topology membrane scission. In press *Nat. Struct. Mol. Biol.*

De Franceschi, N., Alqabandi, M., Miguet, N., Caillat, C., Mangenot, S., Weissenhorn, W. and Bassereau, P. (2019). The ESCRT protein CHMP2B acts as a diffusion barrier on reconstituted membrane necks. *J. Cell Sci.* 132, jcs217968.

Goliand, I., Adar-Levor, S., Segal, I., Nachmias, D., Dadosh, T., Kozlov, M. M. and Elia, N. (2018). Resolving ESCRT-III Spirals at the Intercellular Bridge of Dividing Cells Using 3D STORM. *Cell Rep.* **24**, 1756–1764.

Guizetti, J., Schermelleh, L., Mäntler, J., Maar, S., Poser, I., Leonhardt, H., Müller-Reichert, T. and Gerlich, D. W. (2011). Cortical Constriction During Abscission Involves Helices of ESCRT-III–Dependent Filaments. *Science* **331**, 1616–1620.

Hanson, P. I., Roth, R., Lin, Y. and Heuser, J. E. (2008). Plasma membrane deformation by circular arrays of ESCRT-III protein filaments. *J. Cell Biol.* **180**, 389–402.

Harker-Kirschneck, L., Baum, B. and Šarić, A. (2019). Changes in ESCRT-III filament geometry drive membrane remodelling and fission in silico. *BMC Biol.* **17**, 82.

Henne, W. M., Buchkovich, N. J., Zhao, Y. and Emr, S. D. (2012). The Endosomal Sorting Complex ESCRT-II Mediates the Assembly and Architecture of ESCRT-III Helices. *Cell* **151**, 356–371.

Hierro, A., Sun, J., Rusnak, A. S., Kim, J., Prag, G., Emr, S. D. and Hurley, J. H. (2004). Structure of the ESCRT-II endosomal trafficking complex. *Nature* **431**, 221–225.

Hoffman, H. K., Fernandez, M. V, Groves, N. S., Freed, E. O. and van Engelenburg, S. B. (2019). Genomic tagging of endogenous human ESCRT-I complex preserves ESCRT-mediated membrane-remodeling functions. *J. Biol. Chem.* **294**, 16266–16281.

Hurley, J. H. (2015). ESCRTs are everywhere. *EMBO J.* **34**, 2398–2407.

Hurley, J. H. and Cada, A. K. (2018). Inside job: how the ESCRTs release HIV-1 from infected cells. *Biochem. Soc. Trans.* **46**, 1029–1036.

Im, Y. J. and Hurley, J. H. (2008). Integrated structural model and membrane targeting mechanism of the human ESCRT-II complex. *Dev. Cell* **14**, 902–913.

Jimenez, A. J., Maiuri, P., Lafaurie-Janvore, J., Divoux, S., Piel, M. and Perez, F. (2014). ESCRT Machinery Is Required for Plasma Membrane Repair. *Science* **343**, 1247136.

Johnson, D. S., Bleck, M. and Simon, S. M. (2018). Timing of ESCRT-III protein recruitment and membrane scission during HIV-1 assembly. *Elife* **7**, e36221.

Jouvenet, N., Zhadina, M., Bieniasz, P. D. and Simon, S. M. (2011). Dynamics of ESCRT protein recruitment during retroviral assembly. *Nat. Cell Biol.* **13**, 394–401.

Lata, S., Schoehn, G., Jain, A., Pires, R., Piehler, J., Gottlinger, H. G. and Weissenhorn, W. (2008). Helical structures of ESCRT-III are disassembled by VPS4. *Science* **321**, 1354–1357.

Lee, I.-H., Kai, H., Carlson, L.-A., Groves, J. T. and Hurley, J. H. (2015). Negative membrane curvature catalyzes nucleation of endosomal sorting complex required for transport (ESCRT)-III assembly. *Proc. Natl. Acad. Sci.* **112**, 15892–15897.

Lenz, M., Crow, D. J. G. and Joanny, J.-François (2009). Membrane Buckling Induced by Curved Filaments. *Phys. Rev. Lett.* **103**, 38101.

Maity, S., Caillat, C., Miguet, N., Sulbaran, G., Effantin, G., Schoehn, G., Roos, W. H. and Weissenhorn, W. (2019). VPS4 triggers constriction and cleavage of ESCRT-III helical filaments. *Sci. Adv.* **5**, eaau7198.

Marklew, C. J., Booth, A., Beales, P. A. and Ciani, B. (2018). Membrane remodelling by a lipidated endosomal sorting complex required for transport-III chimera, in vitro. *Interface Focus* **8**, 20180035.

Mast, F. D., Herricks, T., Strehler, K. M., Miller, L. R., Saleem, R. A., Rachubinski, R. A. and Aitchison, J. D. (2018). ESCRT-III is required for scissioning new peroxisomes from the endoplasmic reticulum. *J. Cell Biol.* **217**, 2087–2102.

McCullough, J., Clippinger, A. K., Talledge, N., Skowyra, M. L., Saunders, M. G., Naismith, T. V, Colf, L. A., Afonine, P., Arthur, C., Sundquist, W. I., et al. (2015). Structure and membrane remodeling activity of ESCRT-III helical polymers. *Science* **350**, 1548–1551.

McCullough, J., Frost, A. and Sundquist, W. I. (2018). Structures, Functions, and Dynamics of ESCRT-III/Vps4 Membrane Remodeling and Fission Complexes. *Annu. Rev. Cell Dev. Biol.* **34**, 85–109.

McMillan, B. J., Tibbe, C., Jeon, H., Drabek, A. A., Klein, T. and Blacklow, S. C. (2016). Electrostatic Interactions between Elongated Monomers Drive Filamentation of Drosophila Shrub, a Metazoan ESCRT-III Protein. *Cell Rep.* **16**, 1211–1217.

Mercier, V., Larios, J., Molinard, G., Goujon, A., Matile, S., Gruenberg, J. and Roux, A. (2019). Endosomal Membrane Tension Regulates ESCRT-III-Dependent Intra-Lumenal Vesicle Formation. *bioRxiv* 550483.

Mierzwa, B. E., Chiaruttini, N., Redondo-Morata, L., Moser von Filseck, J., König, J., Larios, J., Poser, I., Müller-Reichert, T., Scheuring, S., Roux, A., et al. (2017). Dynamic subunit turnover in ESCRT-III assemblies is regulated by Vps4 to mediate membrane remodelling during cytokinesis. *Nat. Cell Biol.* **19**, 787.

Muziol, T., Pineda-Molina, E., Ravelli, R. B., Zamborlini, A., Usami, Y., Göttlinger, H. and Weissenhorn, W. (2006). Structural Basis for Budding by the ESCRT-III Factor CHMP3. *Dev. Cell* **10**, 821–830.

Nguyen, H. C., Talledge, N., McCullough, J., Sharma, A., Moss, F. R., Iwasa, J. H., Vershinin, M. D., Sundquist, W. I. and Frost, A. (2020). Membrane constriction and thinning by sequential ESCRT-III polymerization. *Nat. Struct. Mol. Biol.* **27**, 392–399.

Obita, T., Saksena, S., Ghazi-Tabatabai, S., Gill, D. J., Perisic, O., Emr, S. D. and Williams, R. L. (2007). Structural basis for selective recognition of ESCRT-III by the AAA ATPase Vps4. *Nature* **449**, 735–739.

Olmos, Y., Hodgson, L., Mantell, J., Verkade, P. and Carlton, J. G. (2015). ESCRT-III controls nuclear envelope reformation. *Nature* **522,** 236-239.

Olmos, Y., Perdrix-Rosell, A. and Carlton, J. G. (2016). Membrane Binding by CHMP7 Coordinates ESCRT-III-Dependent Nuclear Envelope Reformation. *Curr. Biol.* **26**, 2635–2641.

Pfitzner, A.-K., Mercier, V. and Roux, A. (2019). Vps4 triggers sequential subunit exchange in ESCRT-III polymers that drives membrane constriction and fission. *bioRxiv* 718080.

Prévost, C., AU - Tsai, F.-C., AU - Bassereau, P. and AU - Simunovic, M. (2017). Pulling Membrane Nanotubes from Giant Unilamellar Vesicles. *JoVE* e56086.

Raab, M., Gentili, M., de Belly, H., Thiam, H. R., Vargas, P., Jimenez, A. J., Lautenschlaeger, F., Voituriez, R., Lennon-Duménil, A. M., Manel, N., et al. (2016). ESCRT III repairs nuclear envelope ruptures during cell migration to limit DNA damage and cell death. *Science* **352**, 359–362.

Radulovic, M., Schink, K. O., Wenzel, E. M., Nähse, V., Bongiovanni, A., Lafont, F. and Stenmark, H. (2018). ESCRT-mediated lysosome repair precedes lysophagy and promotes cell survival. *EMBO J.* **37**, e99753.

Reid, E., Connell, J., Edwards, T. L., Duley, S., Brown, S. E. and Sanderson, C. M. (2004). The hereditary spastic paraplegia protein spastin interacts with the ESCRT-III complex-associated endosomal protein CHMP1B. *Hum. Mol. Genet.* **14**, 19–38.

Risa, G. T., Hurtig, F., Bray, S., Hafner, A. E., Harker-Kirschneck, L., Faull, P., Davis, C., Papatziamou, D., Mutavchiev, D. R., Fan, C., et al. (2019). Proteasome-mediated protein degradation resets the cell division cycle and triggers ESCRT-III-mediated cytokinesis in an archaeon. *bioRxiv* 774273.

Rue, S. M., Mattei, S., Saksena, S. and Emr, S. D. (2007). Novel Ist1-Did2 Complex Functions at a Late Step in Multivesicular Body Sorting. *Mol. Biol. Cell* **19**, 475–484.

Samson, R. Y., Obita, T., Freund, S. M., Williams, R. L. and Bell, S. D. (2008). A Role for the ESCRT System in Cell Division in Archaea. *Science* **322**, 1710–1713.

Scheffer, L. L., Sreetama, S. C., Sharma, N., Medikayala, S., Brown, K. J., Defour, A. and Jaiswal, J. K. (2014). Mechanism of Ca2+-triggered ESCRT assembly and regulation of cell membrane repair. *Nat. Commun.* **5**, 5646.

Schöneberg, J., Lee, I.-H., Iwasa, J. H. and Hurley, J. H. (2016). Reverse-topology membrane scission by the ESCRT proteins. *Nat. Rev. Mol. Cell Biol.* **18**, 5.

Schöneberg, J., Pavlin, M. R., Yan, S., Righini, M., Lee, I.-H., Carlson, L.-A., Bahrami, A. H., Goldman, D. H., Ren, X., Hummer, G., et al. (2018). ATP-dependent force generation and membrane scission by ESCRT-III and Vps4. *Science* **362**, 1423–1428.

Shen, Q.-T., Schuh, a. L., Zheng, Y., Quinney, K., Wang, L., Hanna, M., Mitchell, J. C., Otegui, M. S., Ahlquist, P., Cui, Q., et al. (2014). Structural analysis and modeling reveals new mechanisms governing ESCRT-III spiral filament assembly. *J. Cell Biol.* **206**, 763–777.

Shim, S., Kimpler, L. A. and Hanson, P. I. (2007). Structure/Function Analysis of Four Core ESCRT-III Proteins Reveals Common Regulatory Role for Extreme C-Terminal Domain. *Traffic* **8**, 1068–1079.

Skowyra, M. L., Schlesinger, P. H., Naismith, T. V and Hanson, P. I. (2018). Triggered recruitment of ESCRT machinery promotes endolysosomal repair. *Science* **360**, eaar5078.

Sorre, B., Callan-Jones, A., Manneville, J.-B., Nassoy, P., Joanny, J.-F., Prost, J., Goud, B. and Bassereau, P. (2009). Curvature-driven lipid sorting needs proximity to a demixing point and is aided by proteins. *Proc. Natl. Acad. Sci.* **106**, 5622–5626.

Stuchell-Brereton, M. D., Skalicky, J. J., Kieffer, C., Karren, M. A., Ghaffarian, S. and Sundquist, W. I. (2007). ESCRT-III recognition by VPS4 ATPases. *Nature* **449**, 740–744.

Sundquist, W. I. and Kräusslich, H.-G. (2012). HIV-1 Assembly, Budding, and Maturation. *Cold Spring Harb. Perspect. Med.* **2**.

Takahashi, Y., He, H., Tang, Z., Hattori, T., Liu, Y., Young, M. M., Serfass, J. M., Chen, L., Gebru, M., Chen, C., et al. (2018). An autophagy assay reveals the ESCRT-III component CHMP2A as a regulator of phagophore closure. *Nat. Commun.* **9**, 2855.

Tang, S., Henne, W. M., Borbat, P. P., Buchkovich, N. J., Freed, J. H., Mao, Y., Fromme, J. C. and Emr, S. D. (2015). Structural basis for activation, assembly and membrane binding of ESCRT-III Snf7 filaments. *Elife* **4**, e12548.

Teo, H., Veprintsev, D. B. and Williams, R. L. (2004). Structural Insights into Endosomal Sorting Complex Required for Transport (ESCRT-I) Recognition of Ubiquitinated Proteins. *J. Biol. Chem.* **279**, 28689–28696.

Vasan, R., Rudraraju, S., Akamatsu, M., Garikipati, K. and Rangamani, P. (2020). A mechanical model reveals that non-axisymmetric buckling lowers the energy barrier associated with membrane neck constriction. *Soft Matter* **16**, 784–797

Vietri, M., Schink, K. O., Campsteijn, C., Wegner, C. S., Schultz, S. W., Christ, L., Thoresen, S. B., Brech, A., Raiborg, C. and Stenmark, H. (2015). Spastin and ESCRT-III coordinate mitotic spindle disassembly and nuclear envelope sealing. *Nature* **522**, 231–235.

Vietri, M., Radulovic, M. and Stenmark, H. (2020). The many functions of ESCRTs. *Nat. Rev. Mol. Cell Biol.* **21**, 25–42.

von Filseck, J. M., Barberi, L., Talledge, N., Johnson, I., Frost, A., Lenz, M. and Roux, A. (2019). Anisotropic ESCRT-III architecture governs helical membrane tube formation. *bioRxiv* 716308.

Webster, B. M., Colombi, P., Jäger, J. and Lusk, C. P. (2014). Surveillance of Nuclear Pore Complex Assembly by ESCRT-III/Vps4. *Cell* **159**, 388–401.

Wollert, T. and Hurley, J. H. (2010). Molecular mechanism of multivesicular body biogenesis by ESCRT complexes. *Nature* **464**, 864–869.

Wollert, T., Wunder, C., Lippincott-Schwartz, J. and Hurley, J. H. (2009). Membrane scission by the ESCRT-III complex. *Nature* **458**, 172–177.

Yang, D., Rismanchi, N., Renvoise, B., Lippincott-Schwartz, J., Blackstone, C. and Hurley, J. H. (2008). Structural basis for midbody targeting of spastin by the ESCRT-III protein CHMP1B. *Nat. Struct. Mol. Biol.* **15**, 1278–1286.

Yang, B., Stjepanovic, G., Shen, Q., Martin, A. and Hurley, J. H. (2015). Vps4 disassembles an ESCRT-III filament by global unfolding and processive translocation. *Nat. Struct. Mol. Biol.* **22**, 492.

Zamborlini, A., Usami, Y., Radoshitzky, S. R., Popova, E., Palu, G. and Göttlinger, H. (2006). Release of autoinhibition converts ESCRT-III components into potent inhibitors of HIV-1 budding. *Proc. Natl. Acad. Sci.* **103**, 19140 –19145.

This chapter is a modified reproduction of a publication in press:

Pavlin, M.R. and Hurley, J.H. (2020). The ESCRTs: Converging on Mechanism. In press *J. Cell Sci.*

Chapter 2

ATP-dependent force generation and membrane scission by ESCRT-III and Vps4

Abstract

The endosomal sorting complexes required for transport (ESCRTs) catalyze reverse-topology scission from the inner face of membrane necks in HIV budding, multivesicular endosome biogenesis, cytokinesis, and other pathways. We encapsulated ESCRT-III subunits Snf7, Vps24, and Vps2 and the AAA+ ATPase (adenosine triphosphatase) Vps4 in giant vesicles from which membrane nanotubes reflecting the correct topology of scission could be pulled. Upon ATP release by photo-uncaging, this system generated forces within the nanotubes that led to membrane scission in a manner dependent upon Vps4 catalytic activity and Vps4 coupling to the ESCRT-III proteins. Imaging of scission revealed Snf7 and Vps4 puncta within nanotubes whose presence followed ATP release, correlated with force generation and nanotube constriction, and preceded scission. These observations directly verify long-standing predictions that ATP-hydrolyzing assemblies of ESCRT-III and Vps4 sever membranes.

Main Text

Cellular membranes are constantly remodeled in the course of vesicular trafficking, cell division, the egress of HIV, and many other processes. Membranes can bud and be severed either towards or away from the cytosol. The latter is referred to as "reverse topology" scission and is catalyzed by the ESCRT machinery, a set of ~18 proteins in yeast and ~28 in mammals (Campsteijn et al., 2016; McCullough et al., 2013; Olmos and Carlton, 2016; Schöneberg et al., 2016). The core machinery of membrane scission by the ESCRTs consists of the ESCRT-III protein family. The most important components for membrane scission are Snf7, Vps24, and Vps2 (Babst et al., 2002; Teis et al., 2008). When recruited to membranes, ESCRT-III proteins assemble into flat spiral discs (Chiaruttini et al., 2015; Hanson et al., 2008; Shen et al., 2014), helical tubes (Hanson et al., 2008; Lata et al., 2008; McCullough et al., 2015b), or conical funnels (Cashikar et al., 2014; Dobro et al., 2013; McCullough et al., 2015b). ESCRT filaments have a preferred curvature (Chiaruttini et al., 2015; Lenz et al., 2009; Shen et al., 2014). When they are bent to curvatures of higher or lower values, ESCRT filaments act as springs that restore their own shape to the preferred value (Carlson et al., 2015; Chiaruttini and Roux, 2017; Chiaruttini et al., 2015). This spring-like behavior has led to the prediction that ESCRTs could exert measurable forces upon membranes, which we set out to test. The AAA^+ ATPase Vps4 (Babst et al., 1998) is intimately associated with the ESCRT machinery and is essential for the membrane scission cycle. Vps4 is recruited to scission sites by Vps2 (Obita et al., 2007; Stuchell-Brereton et al., 2007). Vps2 is thought to have a capping role whereby it inhibits Snf7 polymerization (Teis et al., 2008). By recycling Vps2 (Mierzwa et al., 2017), Vps4 promotes Snf7 polymerization. Thus, Vps4 is critical for the recycling of ESCRT-III and the replenishment of the soluble cytoplasmic pool. Early attempts at in vitro reconstitution of ESCRT-mediated budding and scission using

giant unilamellar vesicles (GUVs) suggested that the process was independent of Vps4 and ATP (Wollert and Hurley, 2010; Wollert et al., 2009), except for the final post-scission recycling step. Cell imaging studies (Adell et al., 2014; Baumgärtel et al., 2011; Bleck et al., 2014; Elia et al., 2011; Guizetti et al., 2011; Jouvenet et al., 2011), however, showed that Vps4 localization peaked prior to scission in HIV-1 budding and cytokinesis, consistent with its direct role in scission upon ATP hydrolysis. A second goal of this study was to determine if Vps4 and ATP hydrolysis were directly involved in membrane scission, as opposed to mere recycling.

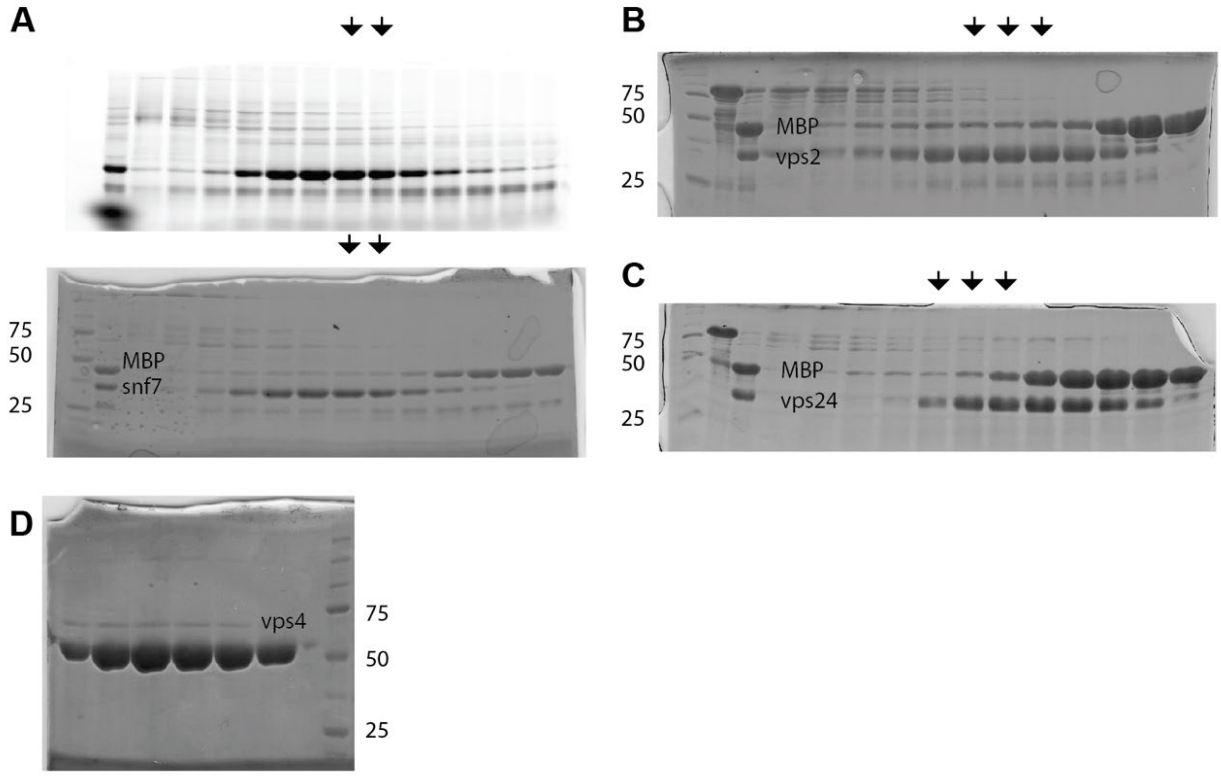

Fig 2.1: **Protein purification.** (A) Cy3B labeled Snf7 after FPLC fractionation on Superdex 75, Typhoon fluorescence scan (top) and Coomassie stain (bottom). (B) Coomassie of Vps2 after FPLC fractionation on Superdex 75. (C) Coomassie of Vps24 after FPLC fractionation on Superdex 75. (D) Coomassie of Vps4 after FPLC fractionation on Superdex 75. Except Vps4, all proteins were expressed as MBP fusion constructs to facilitate expression.

We encapsulated the minimal ESCRT-III-Vps4 module containing yeast Snf7, Vps24, Vps2, and Vps4 (referred to hereafter as the "module;" Fig. 2.1), in POPC:POPS:Biotinyl-PE (80:20:0.1) GUVs at near-physiological ionic strength (~150 mM NaCl; Fig. 2.3 D-G). We used optical tweezers to pull nanotubes extending between the surface of a GUV held by suction on an aspiration pipette and the surface of a streptavidin-coated polystyrene bead held by an optical trap (Fig. 2.3 A-C). To fuel the AAA+ ATPase Vps4, we also encapsulated the caged ATP analog NPE-ATP. An optical fiber was used to UV-illuminate one GUV at a time so that

experiments could be carried out sequentially on individual GUVs in the same microfluidic observation chamber. In control experiments, where all components were included except for ATP, UV illumination led to no change in the force exerted on the bead (Fig. 2.3H, 2.4B). In similar control experiments omitting only Vps4, UV illumination results in a slight drop in the pulling force (Fig. 2.3 I, 2.4C), attributed to the generation of two product molecules upon NPE-ATP uncaging. Thus, in the absence of ESCRT activity the membrane nanotube is stable. When ATP was uncaged in the presence of the complete ESCRT module, a large rise in retraction force was indeed observed (Fig. 2.3 J, 2.4 I). Over ~2-10 min (Fig 2.3 J), the force exceeded the trap maximum of ~65 pN and pulled the bead out of the laser trap. This showed that in the presence of ATP, the ESCRT module can exert forces on membranes.

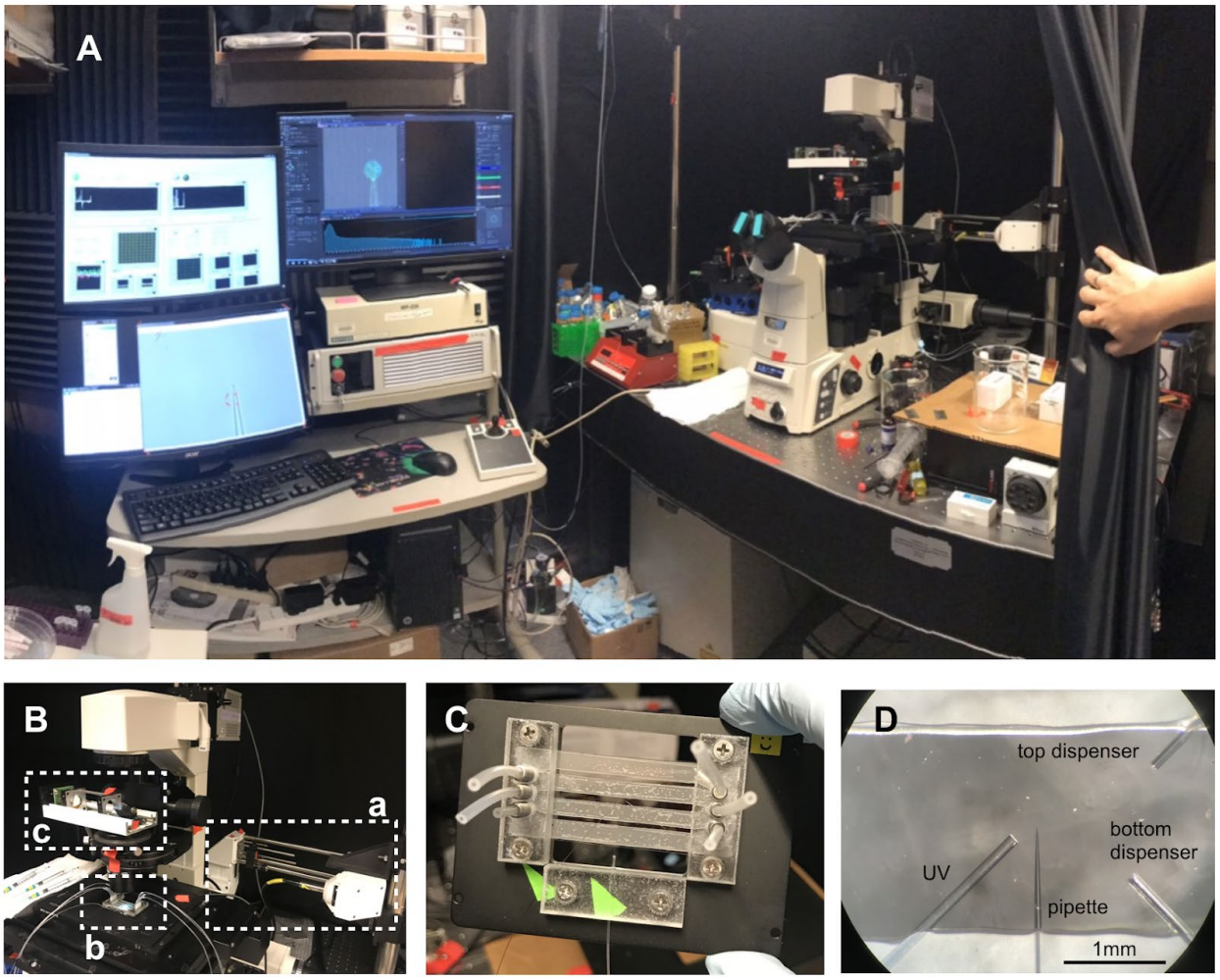

Fig 2.2: **Confleezers setup and microfluidic chamber**. (A) The "Confleezers" combines confocal microscopy, an optical tweezer and microfluidics in one setup. (B) The trap was produced by focusing an IR laser into a high NA, 60x water immersion objective (inset a). The sample was placed in a microfluidics chamber (inset b) to ensure extended time optical tweezing in a debris free environment. Optical trap calibration and force readout was accomplished via back focal plane illumination of a quadrant photodiode (inset c). (C) The microfluidics chamber has three fluid inlets (left), three fluid outlets (right) a fixed UV fiber (bottom left) and a fixed aspiration pipette (bottom right). (D) Zoom into the center of the middle channel of the microfluidics chamber. The chamber

minimized experimental perturbation by separating pulling beads (top channel) and vesicles (bottom channel) from the main channel (middle). Small dispenser tubes connected the top and bottom channel to the main and delivered beads and vesicles individually into the main experimental channel where they were picked up with the trap. Scale bar: 1mm.

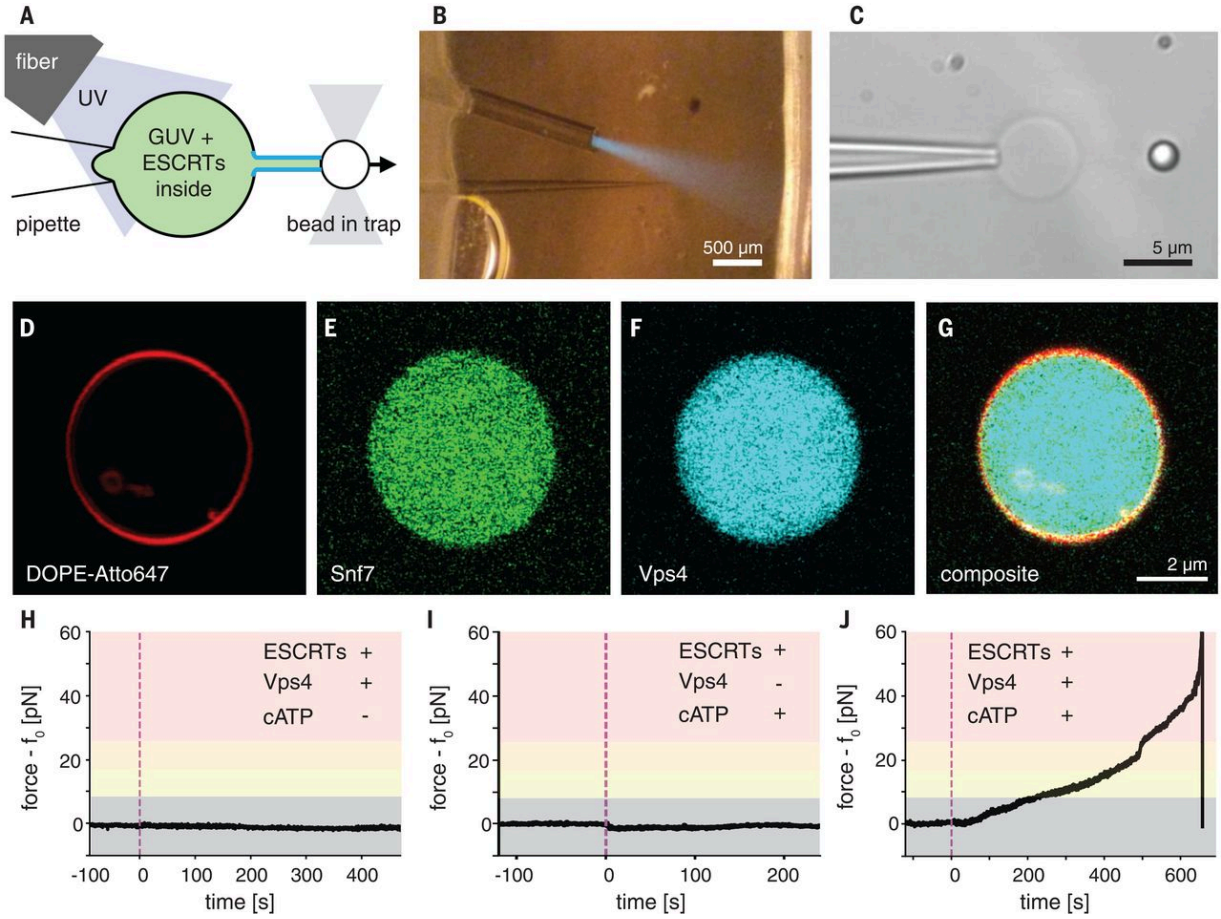

Fig 2.3: ESCRT-III exerts an ATP-dependent force on membrane tubes. (A) Schematic of the experiment: a membrane tube (middle) is pulled out of a micropipette-aspirated GUV with a functionalized bead held in an optical trap, creating a reverse-curvature topology. Components of the ESCRT machinery and caged ATP are encapsulated in the lumen of the GUV. An optical fiber delivers UV light to uncage the ATP inside the vesicle and start the reaction. (B) Aspiration pipette, optical fiber, and UV light cone (blue) inside the microfluidic chamber for our experiments. (C) GUV (center) aspirated by the micropipette (left) and a tube-pulling bead (right). (D to G) Labeling different components of the ESCRT module [membrane label in (D), Snf7 in (E), Vps4 in (F); merged image in (G); 2 µM for all components] revealed a uniform distribution of proteins in the lumen of GUVs. (H to J) Force profiles over time detected by optical tweezers on a membrane tube pulled from a GUV that encapsulates components of the ESCRT module. (H) Control experiment on a full ESCRT module but with ATP omitted. No change in force could be measured. (I) Control experiment on a full ESCRT module but with Vps4 omitted. Apart from a minute dip in the force profile, which was due to small changes in osmolarity upon ATP uncaging, no effects were detected. (J) ATP uncaging (dashed line) in the presence of a full ESCRT module leads to a rise in force exerted on the tube, which is connected to the bead held by the optical trap. A large rise in force can overcome the trapping strength and pull the bead out of the trap.

We sought to determine which components of the ESCRT module were required for force generation (Fig. 2.4 A). With Vps2 or Vps24 as the only ESCRT-III subunits, essentially no force was generated (Fig. 2 4 D,E). In the presence of Snf7, omission of Vps2 or Vps24 led to little or no force generation (Fig. 2.4 F, H), consistent with the role of Vps2 in coupling of ATP hydrolysis by Vps4 to ESCRT-III remodeling, and a role of Vps24 in co-polymerizing with Vps2. When both Vps2 and Vps24 were present, but missing Snf7, a force rise of up to 12 pN was produced, consistent with the ability of Vps24 and Vps2 to co-polymerize (Lata et al., 2008; Mierzwa et al., 2017) (Fig. 2.4 G). The inactivated mutant E233Q of Vps4 (Babst et al., 1998) failed to generate force (Fig. 2.4 J). Deletion of the Vps4-coupling MIM1 motif of Vps2 (Fig. 2.4 K) (Obita et al., 2007; Stuchell-Brereton et al., 2007), which is essential for biological function, abrogated force production. Thus, the ability of the ESCRT module to exert forces on nanotubes, in an ATP-dependent manner (Fig. 2.4 B, C), correlates closely with the presence of all the components that are crucial for ESCRT-mediated membrane scission and their individual integrity (Fig. 2.4 I).

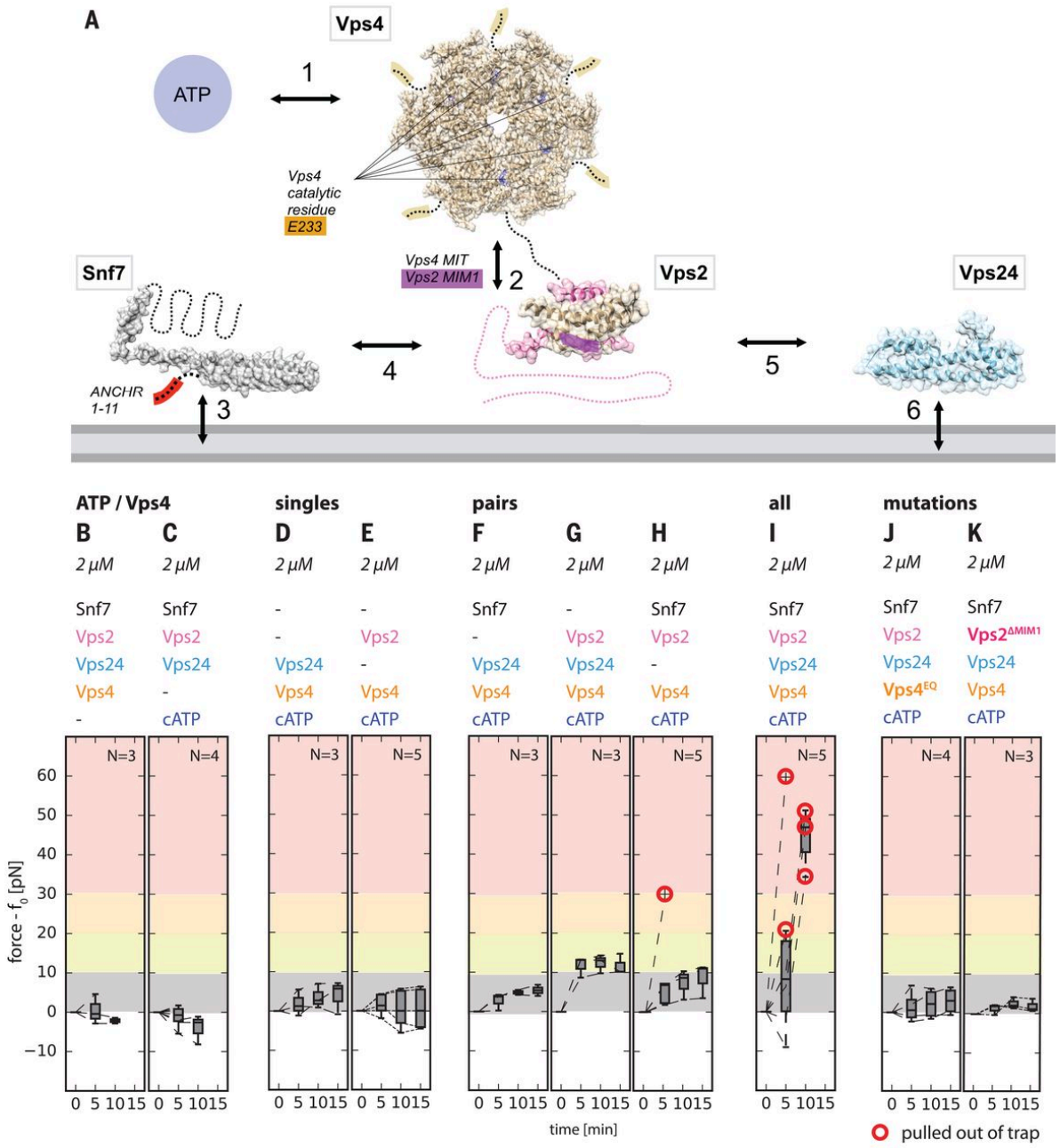

Fig 2.4: Molecular determinants of force generation. (A) Interaction network of the ESCRT module. ESCRT proteins (space-filling structures and dashed lines) interact with the membrane (gray, bottom) as well as with each other. Key components (ATP), catalytic sites, and interacting motifs are highlighted in colors. (B to K) Individual components of the module contributed differently to the force exerted on membrane tubes: ATP and Vps4 were essential for force generation (B and C), and so was ATP hydrolysis (J, catalytically dead Vps4EQ mutant) and critical protein domains (K, Vps2 ΔMIM1). Only the full module (I), or pairings of Vps2 with Vps24 and Snf7 with Vps2 (G and H), led to significant force generation. Our data are consistent with the known interactions underpinning the activity of the ESCRT machinery.

We integrated a confocal microscope with optical tweezing capability to image membrane nanotubes pulled from GUVs containing fluorophore-labeled ESCRTs (Fig. 2.5 A-E, Fig. 2.2).

By pulling on bare membranes, we obtained the bending modulus κ and standardized the calculation of the membrane nanotube radius (Fig. 2.6). To maximize the signal in these experiments, Snf7 was labeled with the photo-stable dye, Lumidyne-550, and imaged with a resonant scanner and a GaAsP detector. We quantitated Snf7, Vps4, and membrane intensity using Gaussian fitting to the diffraction limited tube profile (Fig. 2.7).

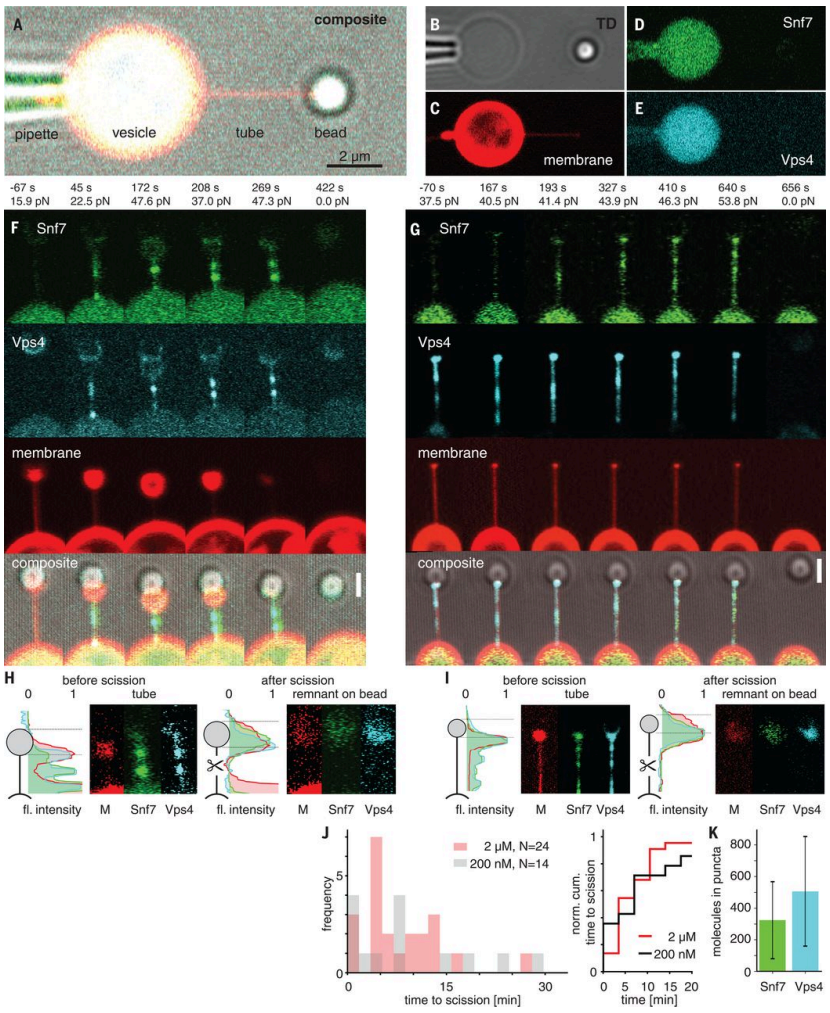

Fig 2.5: Confocal imaging of ATP-dependent membrane tube scission by ESCRTs. (A to E) Micrograph of the experimental setup: the GUV (center, yellow) encapsulating the ESCRT module and caged ATP was aspirated by a micropipette (left). A membrane nanotube was pulled from the GUV using a bead (right) in an optical trap. Membrane, Snf7, and Vps4 are labeled with different fluorophores [composite (A) of individual channels shown in (B to E)]. Scale bar: 2 µm. (F and G) Progression of two representative membrane scission events (2 of 17). UV illumination at *t* = 0 s. Snf7 (green) and Vps4 (cyan) puncta became visible at the vesicle-tube junction and migrated into the tube. Scission happened at ~410 s and ~650 s, respectively. Scale bar: 1.5 µm. (H and I) Tube remnants on the bead identified scission in the middle of the tube. [Brightness adjusted compared to (F) and (G).] (J) Quantification of tube scission. (K) Protein copy numbers in puncta.

We monitored the response of a total of 46 nanotubes pulled from ESCRT module-filled GUVs following UV illumination. The nanotubes manifested a force increase and accumulation

of Snf7 and Vps4 (Fig. 2.5 F-I). Of the 46 trials, 38 (83%) led to scission (Fig. 2.5 J) as judged by simultaneous disappearance of the tube, sudden decrease in the force to zero, and appearance of membrane-, Snf7-, and Vps4-containing remnants on the trapped bead (Fig. 2.5 H, I). Tube lifetimes were widely distributed (Fig. 2.5 J), with a mean lifetime of 425 s before scission. The distributions of lifetimes were similar at the superphysiological concentration of 2 μM, which was used to facilitate visualization, and the near-physiological value of 200 nM (Fig. 2.5 J). One to two diffraction-limited puncta of Snf7 intensity appeared at > 7 SD in 11 out of 17 events analyzed. Typically the puncta nucleated at the tube-vesicle junction (Fig. 2.5F, G). Subsequently, the puncta sometimes moved or disappeared within the tubes. Snf7 puncta were essentially always co-localized with Vps4 (Fig. 2.5F, G). Working at 2 μM, puncta contained in the range of 100-600 copies of Snf7 (Fig. 2.5K), which could exceed the minimum needed for scission, yet is also roughly consistent with estimates in yeast cells (Adell et al., 2017).

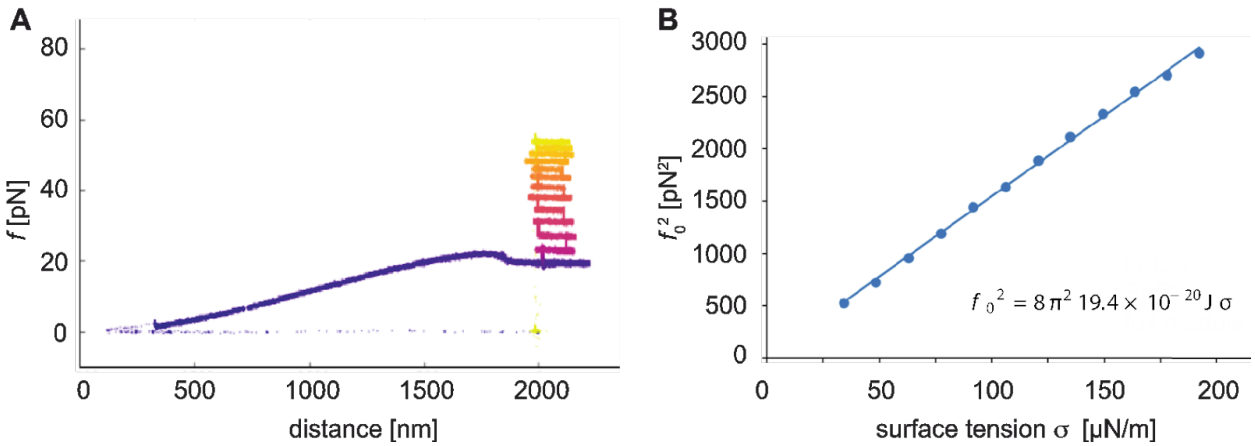

Fig 2.6: **Membrane bending rigidity determination.** (A) A typical tube pulling trace for an empty (no ESCRTs encapsulated) GUV (time in color from blue, early to yellow, late). First the vesicle was approached with the pulling bead (right to left dots on the bottom). Upon touching the surface, pulling on the membrane generated a force (blue line from left to right) as the vesicle was pulled. Above a certain threshold in force a tube was pulled out of the vesicle (hump in the blue curve) and the tube was extended with constant force f_0=20pN. While maintaining a tube, increasing the pipette suction increased the vesicle surface tension, leading to a higher tube force $\bar{\bar{f}}_0 > f_0$. The figure depicts the sampling of increasing suction values and its effect on the tube force (colored vertical lines). (B) The characteristic tube force profile behavior was recorded as the suction pressure was varied. Using the relation $f_0 = 2\pi\sqrt{2\kappa\sigma}$, the bending rigidity κ was determined by fitting. The relation $r_0 = \sqrt{\frac{\kappa}{2\sigma}}$ then gives the corresponding membrane nanotube radius.

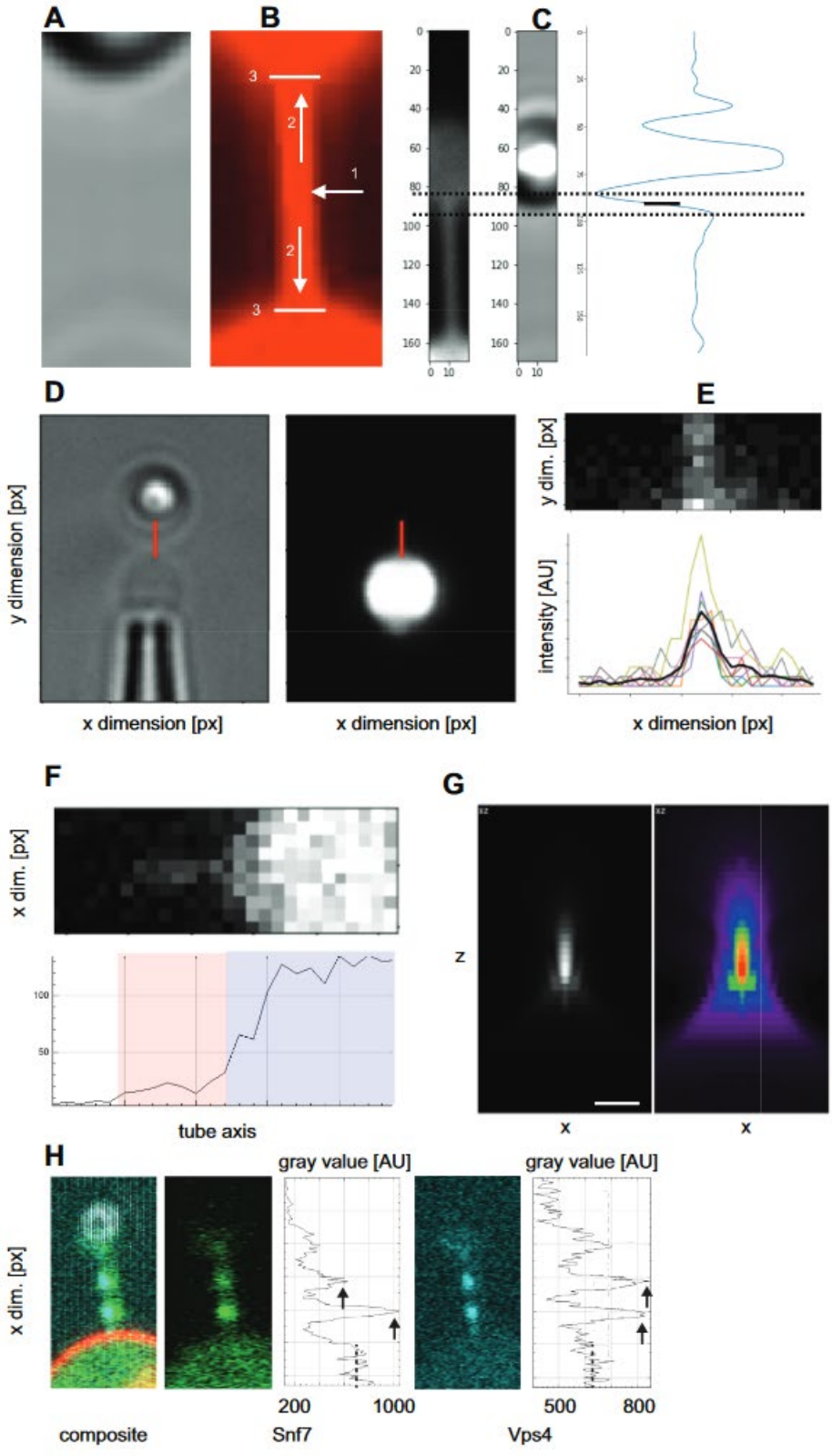

Fig 2.7: Tube vector detection and intensity calculation. For every movie frame, the brightfield channel (A) and the membrane channel (B) were used for vector calculation. In the membrane channel(B), first, the mid-point of

the tube (arrow 1) was found. From there, the length of the tube vector was grown(arrows 2) until the bead or vesicle membrane was reached respectively (arrows 3). C. The position of the bead was determined from the brightfield channel. Along the tube axis, the grey value of the bead showed a characteristic signal. The midpoint (solid line) between the first grey value maximum and first the grey value minimum (dashed lines) was defined as the boundary of the bead. D. The boundary of the bead was found in the grey value histogram as the midpoint between the first minimum and the baseline. The resulting tube vector was plotted over the bright field (left) and membrane channel (right). E. As a diffraction limited line, the tube intensity was calculated by averaging the tube intensity histograms perpendicular to the tube vector (colored) and fitting the resulting histogram (black) with a Gaussian. F and G. Molecular copy number calculation were based on the known internal concentration of single-cysteine labeled proteins and their fluorescence intensity in the vesicle and the tube. F. For quantitation calibration, a rectangular box of the lumen of the GUV was used that is defined in x,y by the image section(F, top and bottom blue) and in z by the optical slice imaged(G)given numerical aperture NA = 0.9, index of refraction n = 1.33, excitation λ = 488 nm, pinhole diameter = 2 µm, and excitation full width half maximum in z = 2.85 µm. From the volume of this box and the protein concentration, the fluorescence intensity to copy number conversion factor was determined. This conversion factor was then used to determine the total number of protein molecules in the tube (F, bottom red) or the total number of protein molecules in a given punctum on the tube. H. Puncta (maxima in the intensity profile on the tube, black arrows) were quantitated based on the above conversion factor and the integrated fluorescence intensity of the puncta.

In order to understand the relationship between the observed force (Fig. 2.8 A, B) and bulk and microscopic properties of the system, we quantitated the nanotube radius over time. Nanotubes used in this study were typically of radius r ~ 20 nm prior to ATP release (Fig. 2.8C, D). The tubes began to narrow almost immediately following ATP release. Narrowing was associated with an increase in the amount of Snf7 and Vps4 seen in the tubes (Fig. 2.8 E, F), whilst essentially no change was seen in the intensity of the GUV membrane or the amount of Snf7 and Vps4 associated with the GUV (Fig. 2.8 G, H). This behavior was consistent over 17 traces (Fig. 2.8 K-N). Final values of r reached 5-10 nm by the time of scission. The uncertainty in the final values of r is substantial because the membrane fluorescence signal is weak when r < 10 nm. In the case of constant membrane tension σ and bending modulus κ, the initial and final force and radius are related to each other by f/fo= r/ro + ro/r/2 and r/ro = f/fo - f/fo2 - 1. Fig. 2.8 A-D shows the values of f (Fig. 2.8 A, B) and r (Fig. 2.8 C, D) computed from the experimental values of r and f, respectively, with no adjustable parameters. The correlation between the measured and computed values is generally excellent (Fig. 2.8 O). Consistent with an apparently constant κ, there is no accumulation of Snf7 on the GUV membrane over the course of the scission events (Fig. 2.8 I). Consistent with a constant σ, the length of the membrane tongue in the pipet was typically constant (Fig. 2.8 J). The formation of ESCRT puncta imposes nanotube radii r smaller than the equilibrium radius r_0, which is associated with an increased pulling force f>fo. These findings are consistent with force generation by punctate microscopic assemblies of ESCRTs within the nanotubes, leading to the constriction of membrane tubes followed by scission.

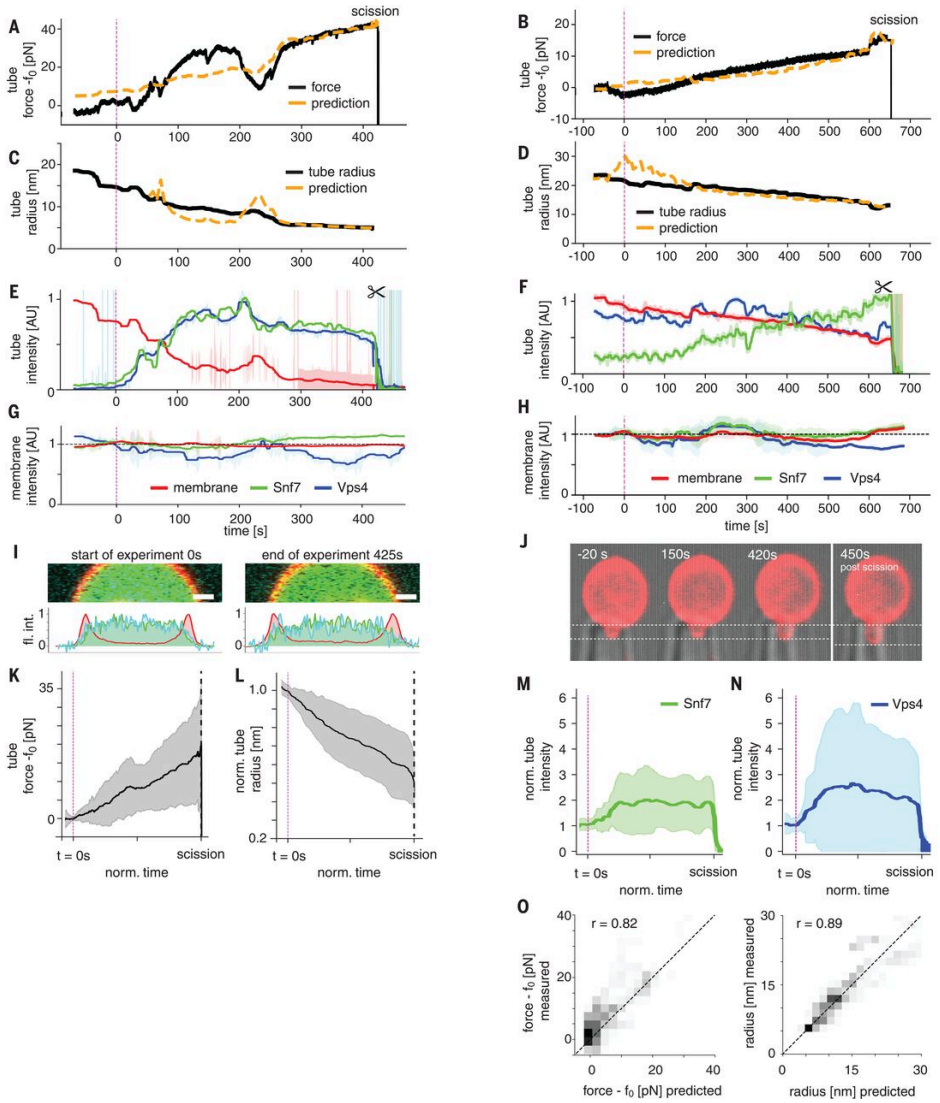

Fig 2.8 ESCRT membrane scission is mediated by tube constriction. (A and B) Force profiles of the same events shown in Fig. 2.5 were normalized to their respective baseline tube holding force, f_0. ATP released by UV uncaging led to a rise in force and eventually scission (indicated by the sharp drop of force at the end of the trace, 2 of 17). (C and D) Simultaneous observation of the tube radius revealed a continuous radius decrease. Force and radius plots are overlaid with predictions from the Helfrich model for a tube of unchanged bending rigidity under constant tension (dashed orange lines) (see methods description in the supplementary material). (E and F) Normalized and bleaching-corrected fluorescence intensity profiles of the scission events for the tube in the three fluorescence channels (Snf7, green; Vps4, cyan; membrane, red). SDs are shown as shaded areas. After ATP uncaging, the tube membrane fluorescence intensity decreased, while the tube Snf7 and Vps4 intensities increased. (G and H) The GUV membrane fluorescence intensity profile over the time course of the scission event was essentially constant and showed no correlation with the force (Snf7, green; Vps4, cyan; membrane, red). SDs are shown as shaded areas. (I) Fluorescence intensity profiles of the GUV membrane at the start and at the end of the scission trace. No increase in protein fluorescence on the membrane was detected. (J) GUV aspiration projection at the beginning, middle, and end of the scission trace, showing essentially no change. (K to N) Averages (N = 17) ± SD of the force, radius, and tube fluorescence showed a consistent force rise, radius decrease, and fluorescence increase in the tube. (O) Correlation (r) between experiments and prediction for radius and force (N = 17).

It has been inferred that the core ESCRT-III proteins Snf7, Vps24, and Vps2, together with Vps4, comprise the minimal ATP-dependent scission machinery (Hanson and Cashikar, 2012; Henne et al., 2013; McCullough et al., 2013; Schöneberg et al., 2016). Here, we directly confirmed this idea by visualizing scission in a minimal system that replicates a wide range of biologically validated structure-function relationships.

The most striking finding from the reconstituted system is that the core ESCRT-III proteins and Vps4 together exert an ATP-dependent axial force on the nanotube before severing. It had previously been proposed (Shen et al., 2014) and then demonstrated (Chiaruttini et al., 2015) that Snf7 filaments have a preferred curvature and may exert forces when bent above or below their preferred value. It had also been hypothesized that breakage or remodeling of ESCRT filaments by Vps4 could contribute to force generation (Carlson et al., 2015; Elia et al., 2012; Mierzwa et al., 2017; Schöneberg et al., 2016). Our observations now provide experimental confirmation that ESCRTs indeed can generate force from within a narrow membrane tube, and show that this force contributes to membrane constriction and is correlated with reverse-topology membrane scission.

ESCRTs (Hanson et al., 2008; Lata et al., 2008; McCullough et al., 2015b) and the "normal topology" scission factor dynamin (Antonny et al., 2016) have been visualized as cylindrical membrane coats, and Snf7 has also been seen in the form of large spirals of hundreds to thousands of copies (Chiaruttini et al., 2015). In the case of dynamin, extended coating of the tube is not needed, and one or a few rings appear capable of mediating scission (Shnyrova et al., 2013). Our measurements of scission by diffraction-limited puncta of Snf7 are consistent with imaging in cells (Adell et al., 2017) and with scission by rings or cones of molecular dimensions. The mechanical nature of constriction and force generation remains to be elucidated through structural approaches.

Materials and Methods

Protein expression, purification and labeling

The following proteins were expressed as N-terminal TEV-cleavable His_6-MBP fusion constructs: Snf7 (N-cys, indicating a cysteine inserted in between the TEV site and the initial methionine), Vps2 (wt and N-cys) and Vps24 (wt and N-cys). Proteins were expressed in *E. coli* Rosetta2 (DE3) cells at 20°C overnight in LB medium. Cell pellets were frozen and stored until use. Pellets were resuspended in Buffer NiW (300 mM NaCl, 50 mM Tris HCl pH 7.4, 10 mM imidazole, 2 mM β-mercaptoethanol (βME)), sonicated, and centrifuged. The supernatant was applied to a gravity column containing 8 ml pre-equilibrated Ni-NTA resin. After washing with NiW buffer, the sample was eluted in 10 ml NiE Buffer (300 mM NaCl, 50 mM TrisHCl pH 7.4, 300 mM imidazole). The eluate was immediately applied to a HiLoad 16/60 Superdex 200 (GE Healthcare, Chicago, IL, USA) chromatography column in buffer S200 (100mM NaCl, 50 mM TrisHCl pH 7.4, 0.1 mM TCEP). Fractions with the highest 280nm absorption were pooled to a total volume of 6 ml and concentration determined from its absorption at 280 nm (NanoDrop spectrophotometer, Thermo Fisher Scientific, Waltham, MA, USA). Labeling was performed by adding 1.5 x molar excess dye (Atto 488 maleimide, Attotec GmbH or Lumidyne 550, Lumidyne Technologies) to the pooled fractions and incubating overnight at 4˚C. As MBP contains no cysteine, only proteins of the ESCRT module were labeled by the dyes. The following day, the

reaction was incubated for 2 h at room temperature with TEV protease (0.65 mg/ml final concentration) and then applied on a HiLoad 16/60 Superdex 75 (GE Healthcare) chromatography column in buffer S75 (300 mM NaCl, 50 mM TrisHCl pH 7.4, 0.1 mM TCEP). The two purest fractions were selected based on SDS-PAGE, read both with a Typhoon for dye absorbance and Coomassie staining, and the concentration determined by Nanodrop. Finally, 3 mM sodium azide was added. Snf7 was always prepared fresh, stored at 4˚C and used within 14 days. Vps2 and Vps24 eluates from the Ni-NTA gravity column were incubated with TEV protease (0.65 mg/ml final concentration) for 2 h at room temperature and then immediately applied to a HiLoad 16/60 Superdex 75 (GE Healthcare) chromatography column in buffer S75 (Fig. 2.1). The purest fractions were pooled and concentrated to stocks of 100-200 µM final concentration, aliquoted, flash frozen in liquid nitrogen and stored at -80˚C until use. For labeling, aliquots were incubated with 2 x molar excess dye (Atto 488 maleimide, Attotec GmbH or Lumidyne 650, Lumidyne Technologies) at 4˚C overnight and desalted with a S75 buffer equilibrated spin column (Biorad) in S75 Buffer.

Vps4 (wt and mutants) was expressed as N-terminal TEV-cleavable His_6 fusion construct. Expression and Ni-NTA steps were done as described above. The Ni-NTA eluate was loaded on a 5 ml HiTrap Q Sepharose Column (GE Healthcare) and eluted with a 0-100% gradient in 12 column volumes from buffer A (50 mM NaCl, 20 mM TrisHCl pH 8.0, 0.1mM TCEP) to buffer B (500 mM NaCl, 20mM TrisHCl pH 8.0, 0.1mM TCEP). The single Vps4 peak was identified by its absorption at 280 nm, pooled and further purified on a HiLoad 16/60 Superdex 75 (GE Healthcare) chromatography column in buffer S75. Vps4 was concentrated to 100 µM, aliquoted and flash frozen in liquid N_2 and stored at -80˚C until use.

Preparation of GUVs

Lipids were purchased from Avanti Polar Lipids (Alabaster, AL). Stock solutions of 10 mg/ml (or lower for the trace components) were prepared by dilution with chloroform. Lipids were mixed at a ratio of 79.1% palmitoyloleoyl-phosphatidylcholine (POPC), 20.5% palmitoyloleoyl-phosphatidylserine (POPS), 0.2% TopFluor-PS or 0.3% dioleoyl-phosphatidylethanolamine (DOPE)-Atto647 (Atto-Tec GmbH) and 0.1 % distearoyl-phosphatidylethanolamine (DSPE)-PEG(2000)-Biotin. 50 µl of the mixture at 3 mg/ml was thinly spread on indium tin oxide (ITO) coated glass slides (Sigma Aldrich). The lipid film was dried for 1 h in a vacuum chamber before being rehydrated in formation buffer. The formation buffer was composed of 150 mM NaCl, 25 mM Tris HCl pH 7.4, 0.05 mM TCEP, 262 mM sucrose. $MgCl_2$ and NPE-caged ATP (adenosine 5'-triphosphate, P3-(1-(2-nitrophenyl)ethyl) ester, disodium salt, Life Technologies) were added to a final concentration of 2 mM. Double distilled H_2O or NaClwere carefully added in trace amounts to reach a total osmolarity of 580 mOsm. For encapsulation at physiological ionic strength (Prévost et al., 2015), purified proteins in buffer were added to reach the following final concentrations: Snf7 2µM, Vps2 2µM, Vps24 2µM and Vps4 2.6µM for the high concentration experiments, each component 10x lower for the low concentration experiments. GUVs were electroformed over 1 h on ice. For all experiments, GUVs were diluted with Buffer S75 at least 1:50.

High precision optical tweezers force measurements

A laser trap on the "mini-tweezers" (Steve B. Smith Engineering, Los Lunas, New Mexico) was formed by focusing two counterpropagating laser beams (λ = 830 nm) through two opposite objective lenses. The force exerted by the nanotube onto a micron-size polystyrene bead trapped by the tweezers was measured by the extent that the laser beams are refracted upon passing through the bead, which were detected by pairs of position sensitive detectors (PSDs). Experiments were performed inside a microfluidic chamber (Fig. 2.2 C) that comprises three channels (top, bottom, and main). Channels were cut into a double layer of plastic film (Nescofilm), which is melted to seal between two microscope cover slides on a hotplate. The channels were connected via glass capillary tubes (i.e. dispenser tubes; King Precision Glass, Claremont, CA, USA). Six holes were drilled into the top cover slide via a laser cutter to allow connection of inlet and outlet tubing to each channel.

We injected 1.56 μm streptavidin-coated beads (Spherotech, Lake Forest, IL, USA) and biotinylated lipid vesicles respectively from the top and bottom channels. At the outlet of the dispenser tubes into the main channel, we trapped individual beads and vesicle and configure them into tube pulling geometry (Sorre et al., 2009) inside the main observation channel (Fig. 2.3 A). An aspiration micro-pipette positioned in the main channel was connected to a high precision pressure controller (MFCS-EZ, 0 to -69 mbar, Fluigent, Villejuif, France), which we use to immobilize a single vesicle on the micro-pipette tip via precise suction control. To release NPE-caged ATP encapsulated inside the vesicle via light activation, we coupled a UV light emitting diode (LED) (Thorlabs, Newton, NJ, USA, λ = 340 nm) to a polarization-resistant multimode optical fiber (Thorlabs) placed right next to the micro-pipette inside the fluidic chamber. We carefully positioned the fiber in such a way that the light cone exiting the fiber (Numerical Aperture 0.22) directly illuminates the vesicle immobilized on the pipette tip (Fig. 2.3 B).

Combined confocal imaging and optical tweezing

We integrated a single optical trap for tweezing onto a commercial confocal imaging system, which we refers to a "Confleezers" (Fig. 2.2 A). The platform was constructed on an inverted microscope unit (motorized Ti-E, Nikon) that contains a stage raiser and an additional (upper) filter cube turret to accommodate and direct the high-power IR laser for trapping. The lower (standard) filter cube turret houses imaging wavelength filters. A Nikon A1R resonant scanning confocal unit was attached to the left camera port of the microscope body. Four solid state lasers (405, 488, 561, 640 nm; LU-N4, Nikon) were paired with appropriate emission filters for fluorescence imaging excitation. A high speed sCMOS camera (ORCA-Flash 4.0 LT, Hamamatsu Photonics) for fast imaging and real-time monitoring of sample manipulation was attached to the right camera port of the scope body and customized to accommodate an IR filter for imaging while trapping. Bright field illumination was provided by the top condenser unit. Wide field fluorescence imaging light was provided from the back side of the microscope (Sola SE II 365, Lumencor). The optical trap was formed by a 5W 1070 nm IR laser (YLR-5-1070-Y12, IPG Photonics). The IR laser's optical fiber output was connected to a laser beam steering optics unit (customized, mirror adjustment and lens collimation units, in parts based on E3300, Elliot Scientific) which was attached to the back side of the scope body through the upper turret. An IR dichroic mirror (Z1064RDC-SP, Chroma) directed the laser to the objective back aperture.

The scope was equipped with a full set of objectives with various magnifications from 10x to 100x.

To form an optical trap at the z-center of the fluidic chamber (i.e. away from the coverslip surface where hydrodynamic interfere is known to compromise the precision of force measurements), an objective with long enough working distance was needed; here we used the Plan Apochromat 60x/1.2NA Water Immersion Objective (MRD07602, Nikon). The position of optical trap z-focus was further carefully aligned to match the z-focus of the scanning confocal unit. A quadrant photodiode (QPD) system (E4100, Elliot Scientific) was attached to the top condenser unit to collect position information of the trapped bead. The refracted IR light from trapped bead was steered and focused on the QPD. QPD voltage outputs were then converted to trapping forces in real time using a custom written software that combines LabView for PC-to-instrument communication and an underlying Python layer for signal processing. Trap stiffness was calculated using the power spectra of position fluctuations of the trapped bead. Imaging is controlled by the imaging software NIS-Elements (Nikon).

The microscope was maintained in a room designed to minimize and to attenuate mechanical and acoustic vibration. A 4' x 6' x 8" tapped optical table (TMC) and a custom-built scope enclosure were used to optimize the stability of our experimental setup. A high-precision xyz piezo stage system (P-545K003, Physik Instrumente GmbH & Co. KG) was installed on top of the general use motorized stage (Ti-S, Nikon) to aide fine manipulation of samples. The stage was machined to accommodate the same microfluidic chambers used in the mini-tweezers (three channels, glued micropipette, and UV optical fiber, see above). Experiments were carried out at room temperature.

Image and data analysis

A baseline recording preceded every force measurement. A linear fit (custom made Python code) was used to capture small drifts in force (due to e.g. immersion water evaporation and resulting coverslip bending relaxation) that were then subtracted from the force trajectory. See supporting information (Fig. 2.6) for membrane parameter calculation. Confocal image stacks of membrane tubes were processed with a suite of custom-made Python scripts as follows: The signal to noise ratio was first improved by applying a walking average over a 20 frame window to the recorded raw data (recorded at 3 frames / s). After bleaching correction, the tube vector (vector between the attachment points on bead and vesicle) was calculated using brightfield and membrane channel for attachment point detection (Fig. 2.7 A-D). The tube fluorescence intensity was then obtained by fitting a Gaussian to the averaged histogram of the diffraction. Quantitation of tube protein fluorescence is based on the known protein concentration in the GUV lumen from which a conversion factor of fluorescence intensity to protein copy number was derived (see Fig. 2.7 F-H). Tube radius was determined based on the tube's fluorescence intensity using a calibration from tubes of known radius (Sorre et al., 2009). For puncta classification, the standard deviation of the background intensity σ_{bg} of the protein channels was calculated and compared with the peak fluorescence intensity of a puncta candidate. A puncta was counted if it was at least 5 pixels wide and its intensity maximum > 7 $\sigma_{bg.}$

Relation between the radius of a membrane tube under tension and the pulling force

According to the model of Derényi et al. (Derényi et al., 2002), which is based on Helfrich's membrane elastic theory, the free energy of a cylindrical membrane tube of radius r and length L under tension subject to a pulling force f is

$$G(r,L) = \left(\frac{\kappa}{2r^2} + \sigma\right) 2\pi r L - fL$$

where κ is the membrane bending rigidity and the pressure-volume term has been neglected. Tension and pulling force are balanced if $\partial G/\partial r = \partial G/\partial L = 0$, which defines the equilibrium radius r0 and force f0,

$$r_0 = \sqrt{\frac{\kappa}{2\sigma}}, \quad f_0 = 2\pi\sqrt{\kappa\sigma}$$

If the radius $_r$ of the tube deviates from r_0, the force f required to balance the tension is given by $\partial G/\partial L = 0$. By using the relations for r_0 and f_0 and after some rearrangements, one obtains the following expression for the force:

$$\frac{f}{f_0} = \frac{1}{2}\left(\frac{r}{r_0} + \frac{r_0}{r}\right).$$

This relation can be inverted to obtain an expression for the tube radius as a function of the force,

$$\frac{r}{r_0} = \frac{f}{f_0} - \sqrt{\frac{f^2}{f_0^2} - 1}\,.$$

We conclude that any deviation of the tube radius $_r$ from $_{r0}$ is associated with an increase in the force.

References

Adell, M. A. Y., Vogel, G. F., Pakdel, M., Müller, M., Lindner, H., Hess, M. W. and Teis, D. (2014). Coordinated binding of Vps4 to ESCRT-III drives membrane neck constriction during MVB vesicle formation. *J. Cell Biol.* **205**, 33–49.

Adell, M. A. Y., Migliano, S. M., Upadhyayula, S., Bykov, Y. S., Sprenger, S., Pakdel, M., Vogel, G. F., Jih, G., Skillern, W., Behrouzi, R., et al. (2017). Recruitment dynamics of ESCRT-III and Vps4 to endosomes and implications for reverse membrane budding. *Elife* **6**, e31652.

Allison, R., Lumb, J. H., Fassier, C., Connell, J. W., Ten Martin, D., Seaman, M. N. J., Hazan, J. and Reid, E. (2013). An ESCRT–spastin interaction promotes fission of recycling tubules from the endosome. *J. Cell Biol.* **202**, 527 LP – 543.

Allison, R., Edgar, J. R., Pearson, G., Rizo, T., Newton, T., Günther, S., Berner, F., Hague, J., Connell, J. W., Winkler, J., et al. (2017). Defects in ER–endosome contacts impact lysosome function in hereditary spastic paraplegia. *J. Cell Biol.* **216**, 1337 LP – 1355.

Antonny, B., Burd, C., De Camilli, P., Chen, E., Daumke, O., Faelber, K., Ford, M., Frolov, V. A., Frost, A., Hinshaw, J. E., et al. (2016). Membrane fission by dynamin: what we know and what we need to know. *EMBO J.* **35**, 2270–2284.

Babst, M., Wendland, B., Estepa, E. J. and Emr, S. D. (1998). The Vps4p AAA ATPase regulates membrane association of a Vps protein complex required for normal endosome function. *EMBO J.* **17**, 2982–2993.

Babst, M., Katzmann, D. J., Estepa-Sabal, E. J., Meerloo, T. and Emr, S. D. (2002). Escrt-III: An endosome-associated heterooligomeric protein complex required for mvb sorting. *Dev. Cell* **3**, 271–282.

Bajorek, M., Morita, E., Skalicky, J. J., Morham, S. G., Babst, M. and Sundquist, W. I. (2009). Biochemical Analyses of Human IST1 and Its Function in Cytokinesis. *Mol. Biol. Cell* **20**, 1360–1373.

Baumgärtel, V., Ivanchenko, S., Dupont, A., Sergeev, M., Wiseman, P. W., Kräusslich, H.-G., Bräuchle, C., Müller, B. and Lamb, D. C. (2011). Live-cell visualization of dynamics of HIV budding site interactions with an ESCRT component. *Nat. Cell Biol.* **13**, 469–474.

Bertin, A., de Franceschi, N., de la Mora, E., Maity, S., Miguet, N., di Cicco, A., Roos, W., Mangenot, S., Weissenhorn, W. and Bassereau, P. (2019). Human ESCRT-III Polymers Assemble on Positively Curved Membranes and Induce Helical Membrane Tube Formation. *bioRxiv* 847319.

Bleck, M., Itano, M. S., Johnson, D. S., Thomas, V. K., North, A. J., Bieniasz, P. D. and Simon, S. M. (2014). Temporal and spatial organization of ESCRT protein recruitment during HIV-1 budding. *Proc. Natl. Acad. Sci.* **111**, 12211 LP – 12216.

Campsteijn, C., Vietri, M. and Stenmark, H. (2016). Novel ESCRT functions in cell biology: spiraling out of control? *Curr. Opin. Cell Biol.* **41**, 1–8.

Carlson, L.-A., Shen, Q.-T., Pavlin, M. R. and Hurley, J. H. (2015). ESCRT Filaments as Spiral Springs. *Dev. Cell* **35**, 397–398.

Cashikar, A. G., Shim, S., Roth, R., Maldazys, M. R., Heuser, J. E. and Hanson, P. I. (2014). Structure of cellular ESCRT-III spirals and their relationship to HIV budding. *Elife* **3**,.

Chang, C.-L., Weigel, A. V, Ioannou, M. S., Pasolli, H. A., Xu, C. S., Peale, D. R., Shtengel, G., Freeman, M., Hess, H. F., Blackstone, C., et al. (2019). Spastin tethers lipid droplets to peroxisomes and directs fatty acid trafficking through ESCRT-III. *J. Cell Biol.* **218**, 2583 LP – 2599.

Chiaruttini, N. and Roux, A. (2017). Dynamic and elastic shape transitions in curved ESCRT-III filaments. *Curr. Opin. Cell Biol.* **47**, 126–135.

Chiaruttini, N., Redondo-Morata, L., Colom, A., Humbert, F., Lenz, M., Scheuring, S. and Roux, A. (2015). Relaxation of Loaded ESCRT-III Spiral Springs Drives Membrane Deformation. *Cell* **163**, 866–879.

De Franceschi, N., Alqabandi, M., Miguet, N., Caillat, C., Mangenot, S., Weissenhorn, W. and Bassereau, P. (2019). The ESCRT protein CHMP2B acts as a diffusion barrier on reconstituted membrane necks. *J. Cell Sci.* **132**, jcs217968.

Delevoye, C., Miserey-Lenkei, S., Montagnac, G., Gilles-Marsens, F., Paul-Gilloteaux, P., Giordano, F., Waharte, F., Marks, M. S., Goud, B. and Raposo, G. (2014). Recycling Endosome Tubule Morphogenesis from Sorting Endosomes Requires the Kinesin Motor KIF13A. *Cell Rep.* **6**, 445–454.

Derényi, I., Jülicher, F. and Prost, J. (2002). Formation and Interaction of Membrane Tubes. *Phys. Rev. Lett.* **88**, 238101.

Dobro, M. J., Samson, R. Y., Yu, Z., McCullough, J., Ding, H. J., Chong, P. L.-G., Bell, S. D. and Jensen, G. J. (2013). Electron cryotomography of ESCRT assemblies and dividing Sulfolobus cells suggests that spiraling filaments are involved in membrane scission. *Mol. Biol. Cell* **24**, 2319–2327.

Eckert, T., Link, S., Le, D. T.-V., Sobczak, J.-P., Gieseke, A., Richter, K. and Woehlke, G. (2012). Subunit Interactions and Cooperativity in the Microtubule-severing AAA ATPase Spastin. *J. Biol. Chem.* **287**, 26278–26290.

Elia, N., Sougrat, R., Spurlin, T. A., Hurley, J. H. and Lippincott-Schwartz, J. (2011). Dynamics of endosomal sorting complex required for transport (ESCRT) machinery during cytokinesis and its role in abscission. *Proc. Natl. Acad. Sci.* **108**, 4846–4851.

Elia, N., Fabrikant, G., Kozlov, M. M. and Lippincott-Schwartz, J. (2012). Computational Model of Cytokinetic Abscission Driven by ESCRT-III Polymerization and Remodeling. *Biophys. J.* **102**, 2309–2320.

Elshenawy, M. M., Kusakci, E., Volz, S., Baumbach, J., Bullock, S. L. and Yildiz, A. (2020). Lis1 activates dynein motility by modulating its pairing with dynactin. *Nat. Cell Biol.* **22**, 570–578.

Guizetti, J., Schermelleh, L., Mäntler, J., Maar, S., Poser, I., Leonhardt, H., Müller-Reichert, T. and Gerlich, D. W. (2011). Cortical Constriction During Abscission Involves Helices of ESCRT-III–Dependent Filaments. *Science* **331**, 1616–1620.

Hanson, P. I. and Cashikar, A. (2012). Multivesicular Body Morphogenesis. *Annu. Rev. Cell Dev. Biol.* **28**, 337–362.

Hanson, P. I., Roth, R., Lin, Y. and Heuser, J. E. (2008). Plasma membrane deformation by circular arrays of ESCRT-III protein filaments. *J. Cell Biol.* **180**, 389–402.

Henne, W. M., Stenmark, H. and Emr, S. D. (2013). Molecular Mechanisms of the Membrane Sculpting ESCRT Pathway. *Cold Spring Harb. Perspect. Biol.* **5**,.

Hurley, J. H. and Yang, D. (2008). MIT Domainia. *Dev. Cell* **14**, 6–8.

Johnson, D. S., Bleck, M. and Simon, S. M. (2018). Timing of ESCRT-III protein recruitment and membrane scission during HIV-1 assembly. *Elife* **7**, e36221.

Jouvenet, N., Zhadina, M., Bieniasz, P. D. and Simon, S. M. (2011). Dynamics of ESCRT protein recruitment during retroviral assembly. *Nat. Cell Biol.* **13**, 394–401.

Lata, S., Schoehn, G., Jain, A., Pires, R., Piehler, J., Gőttlinger, H. G. and Weissenhorn, W. (2008). Helical Structures of ESCRT-III Are Disassembled by VPS4. *Science* **321**, 1354–1357.

Lenz, M., Crow, D. J. G. and Joanny, J.-François (2009). Membrane Buckling Induced by Curved Filaments. *Phys. Rev. Lett.* **103**, 38101.

Mast, F. D., Herricks, T., Strehler, K. M., Miller, L. R., Saleem, R. A., Rachubinski, R. A. and Aitchison, J. D. (2018). ESCRT-III is required for scissioning new peroxisomes from the endoplasmic reticulum. *J. Cell Biol.* **217**, 2087–2102.

McCullough, J., Colf, L. A. and Sundquist, W. I. (2013). Membrane Fission Reactions of the Mammalian ESCRT Pathway. *Annu. Rev. Biochem.* **82**, 663–692.

McCullough, J., Clippinger, A. K., Talledge, N., Skowyra, M. L., Saunders, M. G., Naismith, T. V., Colf, L. A., Afonine, P., Arthur, C., Sundquist, W. I., et al. (2015a). Structure and membrane remodeling activity of ESCRT-III helical polymers. *Sci.* **350**, 1548–1551.

McCullough, J., Clippinger, A. K., Talledge, N., Skowyra, M. L., Saunders, M. G., Naismith, T. V., Colf, L. A., Afonine, P., Arthur, C., Sundquist, W. I., et al. (2015b). Structure and membrane remodeling activity of ESCRT-III helical polymers. *Science* **350**, 1548–1551.

Mierzwa, B. E., Chiaruttini, N., Redondo-Morata, L., Moser von Filseck, J., König, J., Larios, J., Poser, I., Müller-Reichert, T., Scheuring, S., Roux, A., et al. (2017). Dynamic subunit turnover in ESCRT-III assemblies is regulated by Vps4 to mediate membrane remodelling during cytokinesis. *Nat. Cell Biol.* **19**, 787.

Nguyen, H. C., Talledge, N., McCullough, J., Sharma, A., Moss, F. R., Iwasa, J. H., Vershinin, M. D., Sundquist, W. I. and Frost, A. (2020). Membrane constriction and thinning by sequential ESCRT-III polymerization. *Nat. Struct. Mol. Biol.* **27**, 392–399.

Obita, T., Saksena, S., Ghazi-Tabatabai, S., Gill, D. J., Perisic, O., Emr, S. D. and Williams, R. L. (2007). Structural basis for selective recognition of ESCRT-III by the AAA ATPase Vps4. *Nature* **449**, 735–739.

Olmos, Y. and Carlton, J. G. (2016). The ESCRT machinery: new roles at new holes. *Curr. Opin. Cell Biol.* **38**, 1–11.

Pfitzner, A.-K., Mercier, V. and Roux, A. (2019). Vps4 triggers sequential subunit exchange in ESCRT-III polymers that drives membrane constriction and fission. *bioRxiv* 718080.

Prévost, C., Zhao, H., Manzi, J., Lemichez, E., Lappalainen, P., Callan-Jones, A. and Bassereau, P. (2015). IRSp53 senses negative membrane curvature and phase separates along membrane tubules. *Nat. Commun.* **6**, 8529.

Roll-Mecak, A. and Vale, R. D. (2008). Structural basis of microtubule severing by the hereditary spastic paraplegia protein spastin. *Nature* **451**, 363–367.

Schöneberg, J., Lee, I.-H., Iwasa, J. H. and Hurley, J. H. (2016). Reverse-topology membrane scission by the ESCRT proteins. *Nat. Rev. Mol. Cell Biol.* **18**, 5.

Schöneberg, J., Pavlin, M. R., Yan, S., Righini, M., Lee, I.-H., Carlson, L.-A., Bahrami, A. H., Goldman, D. H., Ren, X., Hummer, G., et al. (2018). ATP-dependent force generation and membrane scission by ESCRT-III and Vps4. *Science* **362**, 1423–1428.

Shen, Q.-T., Schuh, a. L., Zheng, Y., Quinney, K., Wang, L., Hanna, M., Mitchell, J. C., Otegui, M. S., Ahlquist, P., Cui, Q., et al. (2014). Structural analysis and modeling reveals new mechanisms governing ESCRT-III spiral filament assembly. *J. Cell Biol.* **206**, 763–777.

Shnyrova, A. V, Bashkirov, P. V, Akimov, S. A., Pucadyil, T. J., Zimmerberg, J., Schmid, S. L. and Frolov, V. A. (2013). Geometric Catalysis of Membrane Fission Driven by Flexible Dynamin Rings. *Science* **339**, 1433–1436.

Simunovic, M., Manneville, J.-B., Renard, H.-F., Evergren, E., Raghunathan, K., Bhatia, D., Kenworthy, A. K., Voth, G. A., Prost, J., McMahon, H. T., et al. (2017). Friction Mediates Scission of Tubular Membranes Scaffolded by BAR Proteins. *Cell* **170**, 172-184.e11.

Sorre, B., Callan-Jones, A., Manneville, J.-B., Nassoy, P., Joanny, J.-F., Prost, J., Goud, B. and Bassereau, P. (2009). Curvature-driven lipid sorting needs proximity to a demixing point and is aided by proteins. *Proc. Natl. Acad. Sci.* **106**, 5622–5626.

Stuchell-Brereton, M. D., Skalicky, J. J., Kieffer, C., Karren, M. A., Ghaffarian, S. and Sundquist, W. I. (2007). ESCRT-III recognition by VPS4 ATPases. *Nature* **449**, 740–744.

Talledge, N., McCullough, J., Wenzel, D., Nguyen, H. C., Lalonde, M. S., Bajorek, M., Skalicky, J., Frost, A. and Sundqust, W. I. (2018). The ESCRT-III proteins IST1 and CHMP1B assemble around nucleic acids. *bioRxiv* 386532.

Teis, D., Saksena, S. and Emr, S. D. (2008). Ordered Assembly of the ESCRT-III Complex on Endosomes Is Required to Sequester Cargo during MVB Formation. *Dev. Cell* **15**, 578–589.

Vietri, M., Schink, K. O., Campsteijn, C., Wegner, C. S., Schultz, S. W., Christ, L., Thoresen, S. B., Brech, A., Raiborg, C. and Stenmark, H. (2015). Spastin and ESCRT-III coordinate mitotic spindle disassembly and nuclear envelope sealing. *Nature* **522,** 231-235.

von Filseck, J. M., Barberi, L., Talledge, N., Johnson, I., Frost, A., Lenz, M. and Roux, A. (2019). Anisotropic ESCRT-III architecture governs helical membrane tube formation. *bioRxiv* 716308.

Wollert, T. and Hurley, J. H. (2010). Molecular mechanism of multivesicular body biogenesis by ESCRT complexes. *Nature* **464**, 864–869.

Wollert, T., Wunder, C., Lippincott-Schwartz, J. and Hurley, J. H. (2009). Membrane scission by the ESCRT-III complex. *Nature* **458**, 172–177.

Yang, D., Rismanchi, N., Renvoisé, B., Lippincott-Schwartz, J., Blackstone, C. and Hurley, J. H. (2008). Structural basis for midbody targeting of spastin by the ESCRT-III protein CHMP1B. *Nat. Struct. Mol. Biol.* **15**, 1278–1286.

Zamborlini, A., Usami, Y., Radoshitzky, S. R., Popova, E., Palu, G. and Göttlinger, H. (2006). Release of autoinhibition converts ESCRT-III components into potent inhibitors of HIV-1 budding. *Proc. Natl. Acad. Sci.* **103**, 19140–19145.

Acknowledgments: We thank J.-Y. Lee, H. Aaron, S. Ruzin and D. Schichnes for assistance with imaging, M. Vahey, D. Fletcher, and P. Lishko for advice on the aspiration pipette set-up, A. Lee for assistance with the optical trap force calibration and C. Glick for advice with the microfluidics.

This chapter is a modified reproduction of

Schöneberg, J., Pavlin, M. R., Yan, S., Righini, M., Lee, I.-H., Carlson, L.-A., Bahrami, A. H., Goldman, D. H., Ren, X., Hummer, G., et al. (2018). ATP-dependent force generation and membrane scission by ESCRT-III and Vps4. *Science* **362**, 1423–1428.

Chapter 3

CHMP1B, IST1, and Spastin Constitute a Novel Membrane Scission Machinery

Abstract

The ESCRT proteins are involved in a large number of membrane remodeling functions in a reverse topology, scissioning membranes away from the cytosol. However, various reports have suggested possible roles for ESCRTs in normal topology membrane processes. Here, we report a novel function for CHMP1B, IST1, and Spastin in the remodeling and scission of membrane nanotubes. We further show that Spastin is capable of fully disassembling CHMP1B homopolymers and CHMP1B-IST1 heteropolymers. Together, these results suggest that CHMP1B, IST1, and Spastin constitute a novel ESCRT machinery capable of remodeling and scissioning membranes in a normal topology.

Introduction

For decades the ESCRT machinery was understood to be a membrane remodeling machinery that scissions membranes away from the cytosol. This understanding was challenged by a landmark study that revealed new ESCRT homo-and-hetero polymers of CHMP1B and IST1 that could tubulate membranes in a normal topology (McCullough et al., 2015). High resolution electron microscopy showed these polymers to constrict membranes nearly to the point of hemi-fission (McCullough et al., 2015; Nguyen et al., 2020). Furthermore, overexpressed CHMP1B and IST1 *in vivo* resulted in tubular invaginations of the plasma membrane (McCullough et al., 2015), suggesting that this polymer could be physiologically relevant. With recent reports hinting at multiple roles for ESCRTs in "normal topology" scission (Allison et al., 2013; Bertin et al., 2019; McCullough et al., 2015; von Filseck et al., 2019), a deeper understanding of the mechanism and physiological role for this polymer is critical to understanding the myriad functions of the ESCRTs.

CHMP1B and IST1 are ESCRT-III proteins most prominently known for their roles in cytokinesis, in which CHMP1B and IST1 recruit the AAA+ ATPase Spastin to sever microtubules and resolve the cytokinetic bridge (Vietri et al., 2015; Yang et al., 2008). Spastin is recruited though its Microtubule Interacting and Trafficking (MIT) domain, which binds with various affinity to MIT-Interacting Motifs (MIMs) common in ESCRT-III proteins (Bajorek et al., 2009; Hurley and Yang, 2008). CHMP1B contains a type 1 MIM in its C-terminus (Yang et al., 2008), through which it recruits Spastin during cytokinesis, while IST1 encodes both a type 1 and a type 2 MIM (Bajorek et al., 2009), whose functions have not yet been elucidated.

CHMP1B and IST1 have been shown to be crucial in the proper lysosome function (Allison et al., 2017), regulation and scissioning of endosomal recycling tubules (Allison et al., 2013) which are responsible for recycling cargo from endosomes to the plasma membrane and the golgi (Allison et al., 2013), and ensuring proper lipid metabolism through peroxisome-lipid

droplet contacts (Chang et al., 2019). Interestingly, the scission of endosomal recycling tubes presumably occurs in a normal-topology fashion, and such membrane nanotubes could serve as a template for CHMP1B-IST1 polymers. Endosomal recycling tubes are closely linked to nearby microtubules, both of which are regulated by Spastin (Allison et al., 2013), and defects in the function of Spastin or IST1, and to a lesser degree CHMP1B, lead to an overabundance of recycling tubules unable to fission (Allison et al., 2013).

Taken together these observations raise an exciting model: CHMP1B and IST1 are capable of polymerizing onto tubular membranes, and, in conjunction with Spastin, scissioning these tubules. We thus set out to reconstitute CHMP1B-IST1 tubes and study their function on pulled membrane nanotubes, as well as elucidate the interactions between CHMP1B, IST1, and Spastin.

Results

We first set out to visualize the activity of CHMP1B and IST1 on pulled membrane nanotubes. We purified full-length CHMP1B and the IST1 N-terminal Domain (NTD), both modified with an N-terminal cysteine to facilitate fluorescent labelling. ESCRT-III proteins are auto-inhibited by their c-termini (Zamborlini et al., 2006), and IST1 NTD has been shown to more readily polymerize than the full-length version. We set out to test CHMP1B and IST1 activity on mechanically extruded membrane nanotubes using our custom confocal microscope described previously (Schöneberg et al., 2018). For normal-topology scission where proteins are external to the GUV lumen, we required a mechanism to flow protein into the chamber. We thus modified our microfluidic chambers to include an additional injection pipette in place of the UV-fiber previously used (Schöneberg et al., 2018), connected to a syringe pump capable of achieving very low flow rates. GUVs and beads were flown into the chamber and a nanotube was extruded as described previously (Schöneberg et al., 2018), after which protein was slowly injected using the syringe pump. As protein density slowly accumulated on the tube, the bead was moved away from the GUV, to induce friction on the membrane. Shortly after, the nanotube was observed to scission at its neck and retract to the bead (Fig 3.1)

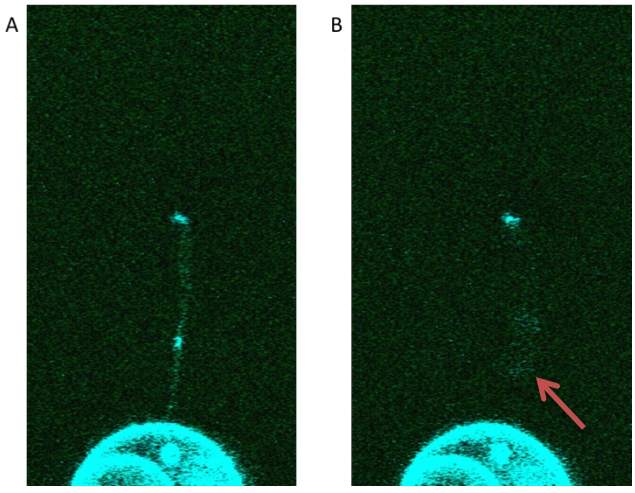

Fig 3.1: Membrane nanotube scission. CHMP1B and IST1 polymerize on the nanotube. Inducing friction by pulling the bead away from the GUV seems to induce scission of the tube neck, followed by retraction. Red

arrow indicates the post-scission membrane tube retracting. Membrane is colored blue and CHMP1B is colored green.

However, our sealed microfluidic chamber made interpretation of this experiment difficult due to significant mechanical force imparted on the system from the flow generated by the injection pipette. Flow rates low enough to not exert mechanical force required excessive dwell time from extruding the nanotube to protein arriving. We therefore conducted these experiments on a collaborator's instrument, which used micromanipulators in place of a microfluidic chamber, and an unsealed, large volume chamber which rendered flow effects negligible. We aspirated GUVs with one micromanipulator, while injecting protein with the other. The optical trap held a streptavidin-functionalized polystyrene bead, which was used to extrude a membrane nanotube from the GUV using biotinylated lipids, similar to previous work (Schöneberg et al., 2018). After extruding a membrane nanotube, CHMP1B and IST1 were briefly locally injected onto the tube with the aid of a second pipette. Protein began to rapidly accumulate on the tube, nucleating on the neck and growing outward. After pulling the nanotube further from the GUV by moving the bead away, new protein was observed nucleating at the neck (Fig 3.2 C), and scission of the nanotube soon follows.

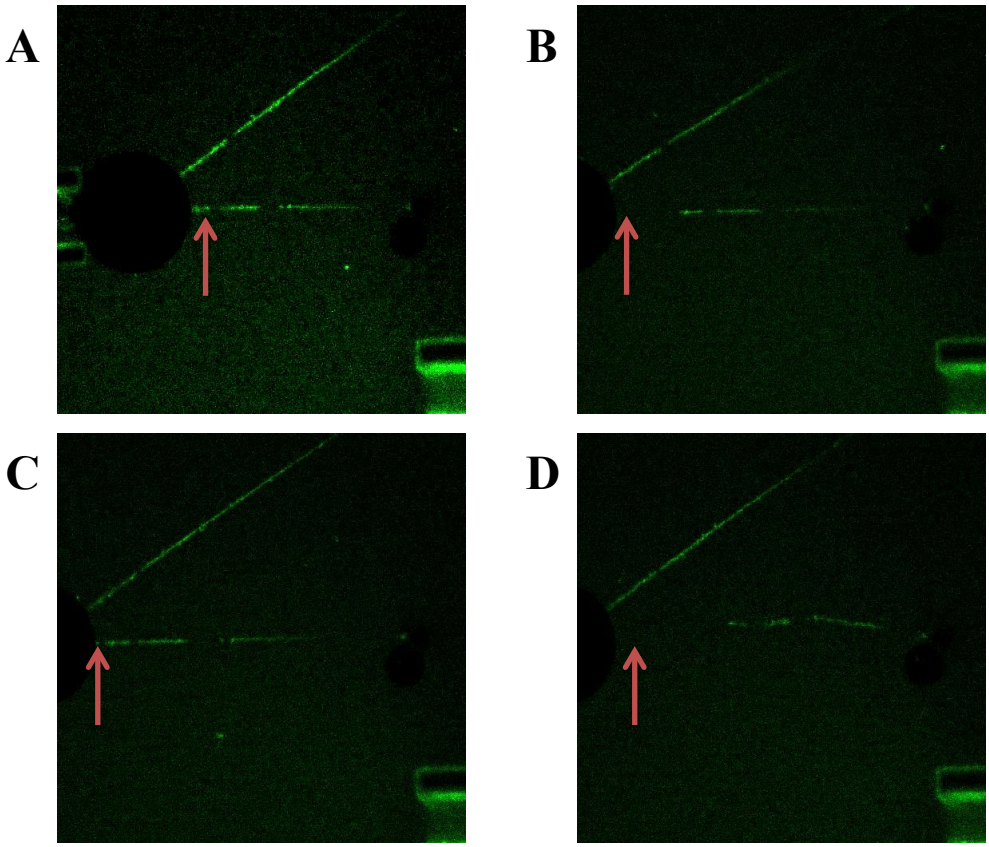

Fig 3.2: CHMP1B and IST1 scission membrane nanotubes. (A) CHMP1B and IST1 are injected by a pipette (bottom right) onto a membrane nanotube extruded by a bead held in an optical trap. CHMP1B is fluorescently labelled. A

second nanotube, above, was extruded by a residual attachment to the coverslip when the GUV was aspirated. (B) The bead is pulled slightly further from the GUV, lengthening the nanotube. (C) The nanotube begins retracting into the GUV, while new protein nucleates at the neck. (D) Scission occurs at the neck of the nanotube, and the nanotube and protein retract toward the bead. The red arrow tracks the location of the nanotube neck.

Interestingly, immediately after lengthening the nanotube by moving the bead further from the GUV, the nanotube began to retract back into the GUV. This retraction was slowed, and ultimately halted, coincident with new protein density forming on the neck. Scission followed immediately after, with the nanotube retracting to the nanoparticle.

In order to visualize both CHMP1B and IST1 simultaneously we repeated the experiment on a second confocal modified with three micromanipulators. The GUV and nanoparticle were each aspirated by separate micromanipulators, with the third injecting protein onto the extruded membrane nanotube. We allowed protein to accumulate on the nanotube, verifying co-localization of CHMP1B and IST1, after which the GUV was pulled away from the nanoparticle. The nanotube once again scissioned its neck and retracted to the bead, leaving a small protein puncta at the scissioned nanotube-GUV junction (Fig 3.3).

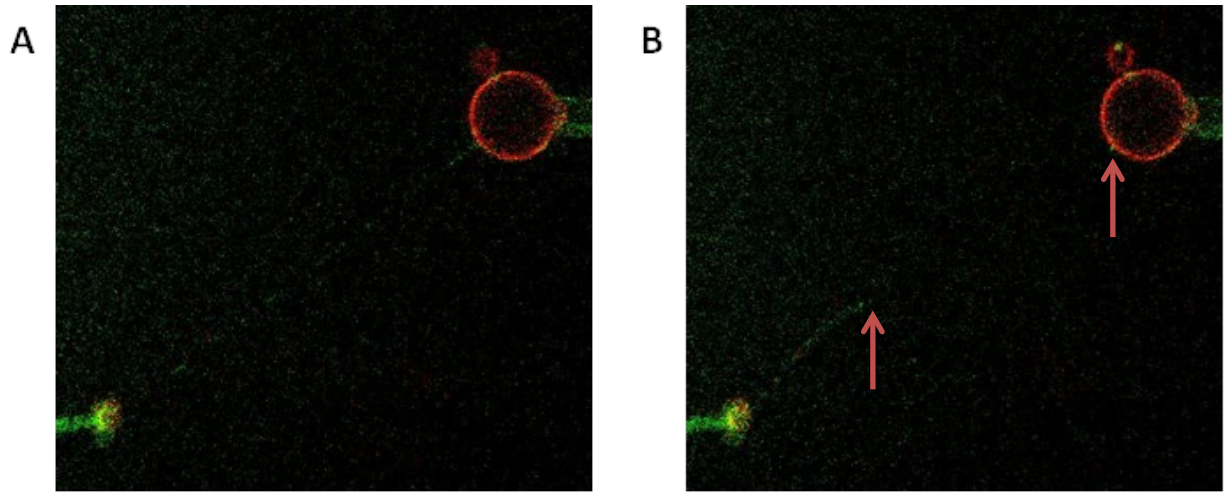

Fig 3.3: Reproducing Scission. CHMP1B and IST1 assemble on the nanotube. After lengthening the nanotube by pulling the GUV away from the nanoparticle, the nanotube scissions and retracts to the nanoparticle. (A) Prior to scission (B) Post-Scission. Arrows indicate the protein puncta remaining on the neck, and the end of the retracting nanotube.

It has been shown that diffusely-bound protein can form a partial diffusion barrier for lipids if dense enough (De Franceschi et al., 2019; Simunovic et al., 2017). We therefore reasoned that a rigid CHMP1B-IST1 polymer would prevent retraction of the nanotube into the GUV if the bead were released from the optical trap. We extruded a nanotube, injected CHMP1B and IST1 onto it, then released the nanoparticle from the optical trap (Fig 3.4). Indeed, after release the nanotube failed to retract, with uncoated membrane crumpling while protein-coated membrane remained rigid, supporting the idea that CHMP1B-IST1 are forming the polymer tubes observed previously.

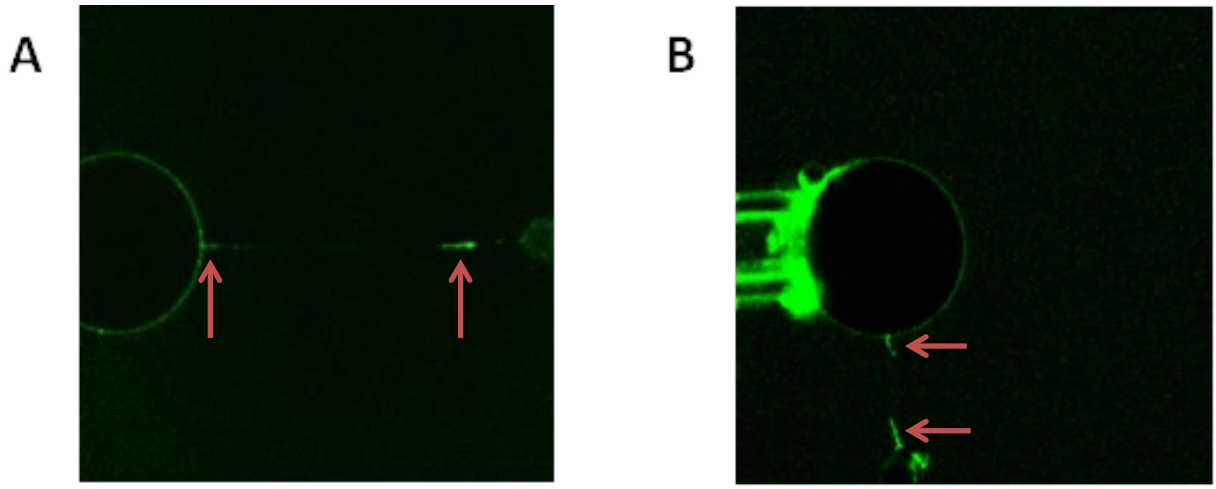

Fig 3.4: CHMP1B-IST1 form rigid diffusion barriers on membrane nanotubes. (A) Prior to releasing the nanoparticle. (B) After releasing the nanoparticle. Red arrows indicate rigid protein assemblies.

In canonical ESCRT processes VPS4 activity is crucial to ESCRT-III remodeling and scission (Henne et al., 2013; Johnson et al., 2018; Lata et al., 2008; Pfitzner et al., 2019), where VPS4 acts to remodel ESCRT polymers in a process thought to drive membrane constriction and scission. Since IST1 and CHMP1B recruit Spastin to several areas of membrane remodeling activity (Allison et al., 2013; Chang et al., 2019; Vietri et al., 2015; Yang et al., 2008), we asked whether Spastin serves an analogous role for CHMP1B-IST1 polymers. We therefore next sought to test Spastin interaction on CHMP1B-IST1 polymers *in vitro*.

Spastin is expressed predominantly as two isoforms. Full-length Spastin includes an N-terminal transmembrane domain which tethers it to endosomal membranes (Roll-Mecak and Vale, 2008). An alternatively translated isoform, M87 Spastin, is cytosolic, and demonstrates no loss of microtubule–severing function (Roll-Mecak and Vale, 2008). We therefore expressed and purified M87 Spastin. To verify Spastin activity, we first sought to reproduce Spastin's ATP-dependent microtubule-severing activity. We used a total-internal reflection microscopy (TIRF) assay to test whether purified M87 could recycle microtubules adhered to a glass coverslip. Adhered microtubules were treated with either buffer or 1um Spastin and imaged continuously for 2 minutes. Control microtubules showed no change, while microtubules treated with Spastin were rapidly recycled with no observable microtubules after 1 minute (Fig 3.5).

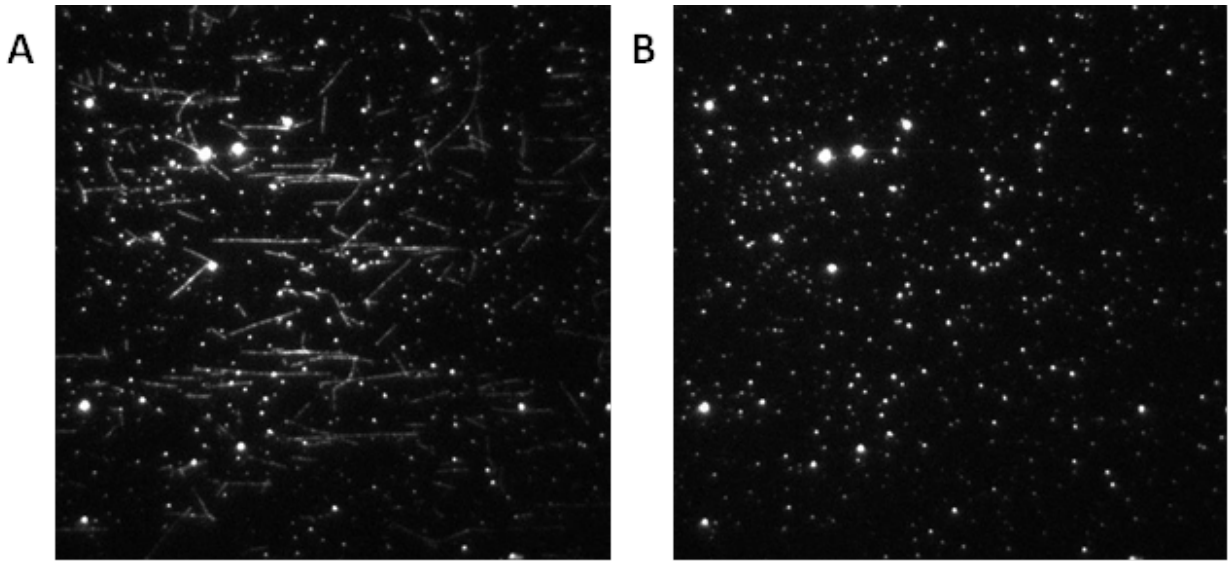

Fig 3.5: Spastin Recycles Microtubules *in vitro*. (A) Microtubules adhered to a glass surface treated with buffer. (B) Microtubules treated with Spastin after 1 minute incubation. No visible microtubules remain.

Having verified Spastin's activity on microtubules, we next sought to test Spastin activity on CHMP1B-IST1 polymers, we generated CHMP1B-IST1 *in vitro* using highly negatively charged Small Unilamellar Vesicles (SUVs) to nucleate polymer assembly. We verified successful assembly using negative-stain electron microscopy (EM) (Fig 3.6).

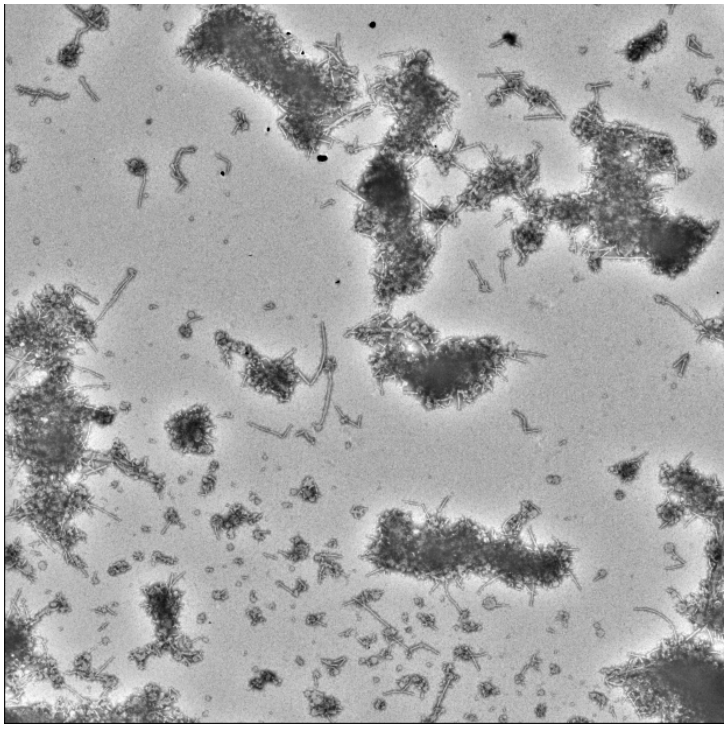

Fig 3.6: High Yield Assembly of CHMP1B *in vitro.* CHMP1B and IST1 nucleate on highly negatively charged small unilammelar vesicles (SUVs), with infrequent non-membrane-bound tubes observed.

Next, we tested whether these tubes could be disassembled by Spastin. We allowed fluorescent CHMP1B-IST1 assemblies to settle to the bottom of a Lab-Tek chamber and imaged the assemblies under confocal microscopy. After the assemblies had fully settled, Spastin and ATP were added carefully in bulk to not disturb the assemblies (Fig 3.7).

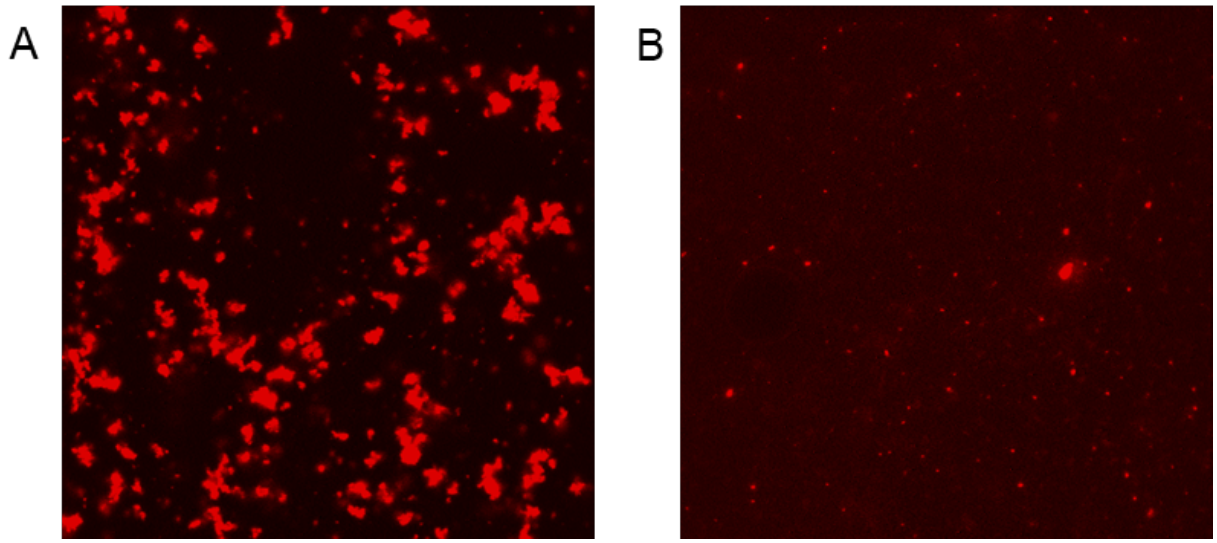

Fig 3.7: Spastin Disassembles CHMP1B-IST1 Assemblies. (A) Assemblies settled in the chamber (B) Assemblies after 5 minute incubation with Spastin.

To study the disassembly more quantitatively, we performed a pelleting assay: assembled tubes were gently pelleted by centrifugation, after which the supernatant was removed and the tubes resuspended in buffer. Tubes were then treated either with buffer, Spastin with ATP/Magnesium, or Spastin with EDTA for 10 minutes. Samples were then pelleted and the supernatant gently aspirated so as not to disturb the protein pellet. The supernatants and pellets were run on SDS-PAGE gels, and the band intensities quantified (Fig 3.8).

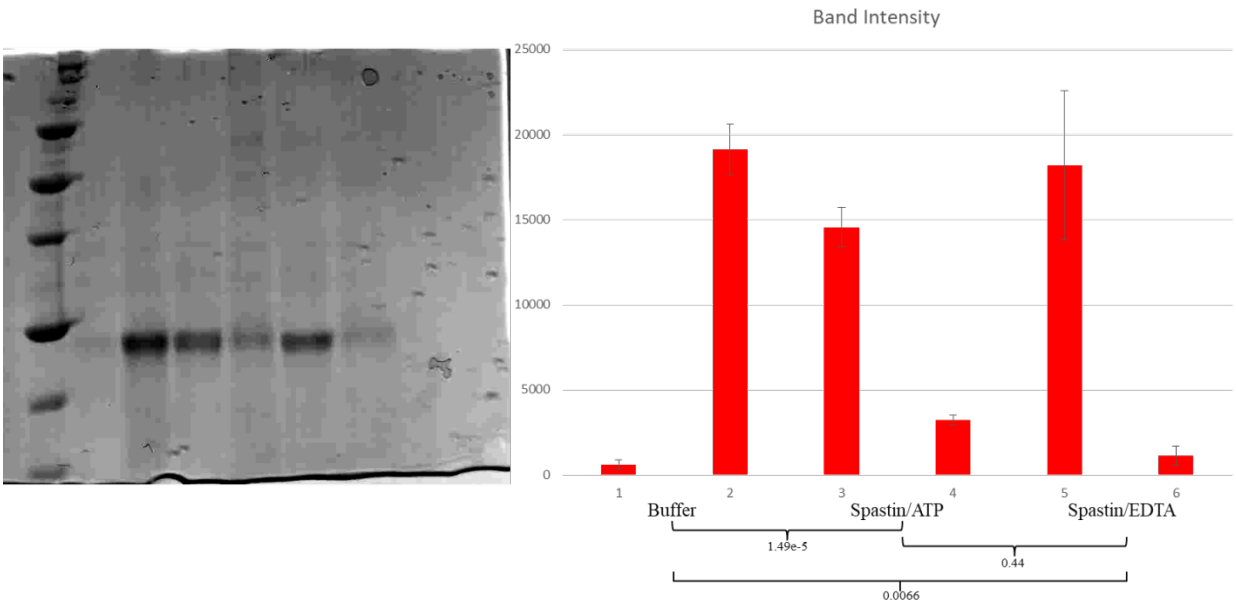

Fig 3.8: Spastin Recycles CHMP1B-IST1 Tubes. Disassembly assay of CHMP1B-IST1 tubes. B – Buffer Only; S – Spastin/ATP; E-Spastin/EDTA; S – Supernatant; P – Pellet. P-values B->S, B->E, S->E are 4.5e-05, 1.4e-05, and .87, respectively.

In sample treated with buffer only the tubes remain entirely in the pellet fraction, indicating no resolubilization or spontaneous disassembly. However, when treated with Spastin either with or without EDTA the tubes were disassembled and the subunits recycled to the supernatant nearly completely, suggesting that Spastin recycles CHMP1B-IST1 tubes in a non-ATP dependent manner. We reasoned that this disassembly must be driven through the interaction of Spastin's MIT domain with CHMP1B's MIM domain, since the IST1 NTD construct's MIMs are truncated. We therefore repeated the experiment for CHMP1B homopolymers to test whether Spastin interacts with the polymers through CHMP1B's MIM motif (Fig 3.9).

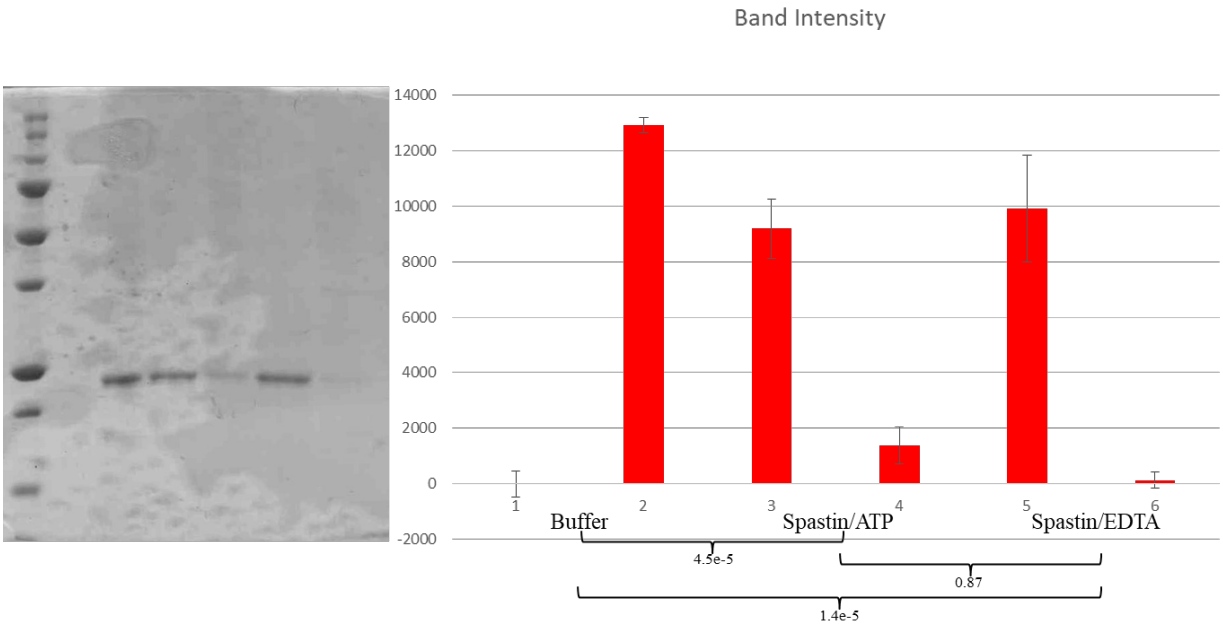

Fig 3.9: CHMP1B Homopolymers Are Disassembled by Spastin. CHMP1B homopolymers show similar disassembly to CHMP1B-IST1 heteropolymers. P-values are labelled below.

CHMP1B homopolymers show identical disassembly by Spastin, in a non-ATP dependent manner, as IST1 heteropolymers.

Finally, we turned to cryo-EM to visualize the molecular mechanism by which Spastin disassembles CHMP1B and CHMP1B-IST1 polymers. We set out to perform a time-course disassembly assay to catch intermediary states of polymer disassembly. To perform the time-course disassembly, assembled CHMP1B-IST1 tubes were applied to glow-discharged C-flat 2/1 300 mesh grids followed by either buffer or 1uM Spastin. The disassembly was halted by blotting and plunge freezing after either 30 seconds or 5 minutes, and the samples imaged (Fig 3.10).

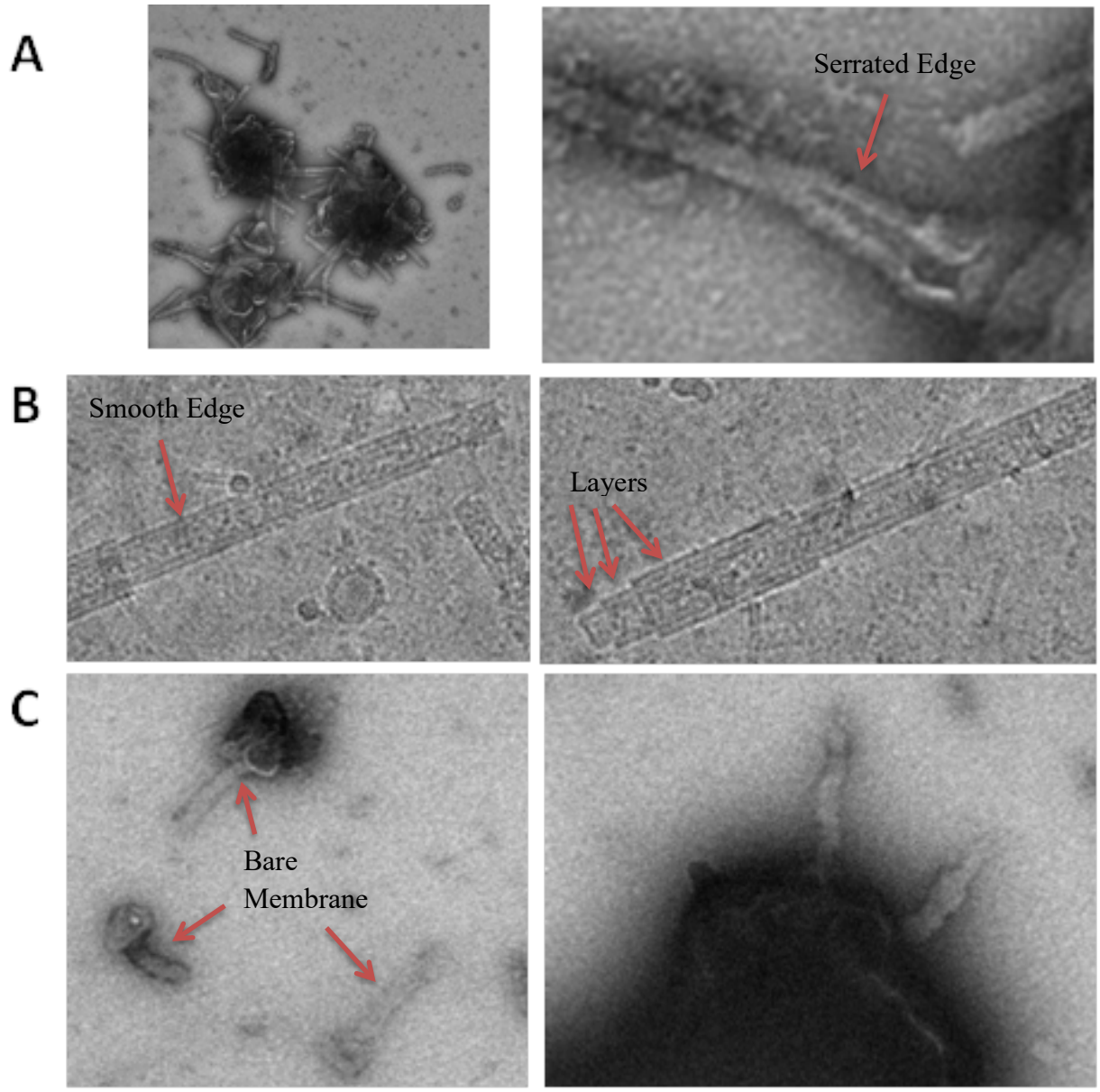

Fig 3.10: Disassembly Time-Course of CHMP1B-IST1 Tubes. (A) Buffer only. Heteropolymer assemblies are frequently observed tubulating SUVs. As has been observed previously, CHMP1B homopolymers and CHMP1B-IST1 heteropolymers have distinct, serrated edges, while IST1 homopolymers have a distinctly smooth edge. (B) 30 second disassembly. No heteropolymers are observed. IST1 homopolymers, and multi-layered homopolymers, are observed sparsely. (C) 5 minute disassembly. No polymers are observed. Bare membrane protrusions are observed, often with protein aggregates surrounding them.

As has been noted previously (McCullough et al., 2015), CHMP1B homopolymers and heteropolymers can be distinguished from IST1 homopolymers at low resolution by their distinct serrated edge, while IST1 homopolymers have a distinctly smooth edge. In the buffer only sample, heteropolymers predominate and are abundant. In the 30 second sample only sparse IST1 homopolymers are observed, often apparently with multiple layers of IST1. In the 5 minute sample no protein polymers are observed, though bare membrane protrusions emanating from

SUVs are frequently observed. Spastin was not observed decorating the IST1 homopolymers, though hexameric Spastin was observed in close proximity to one (Fig 3.11).

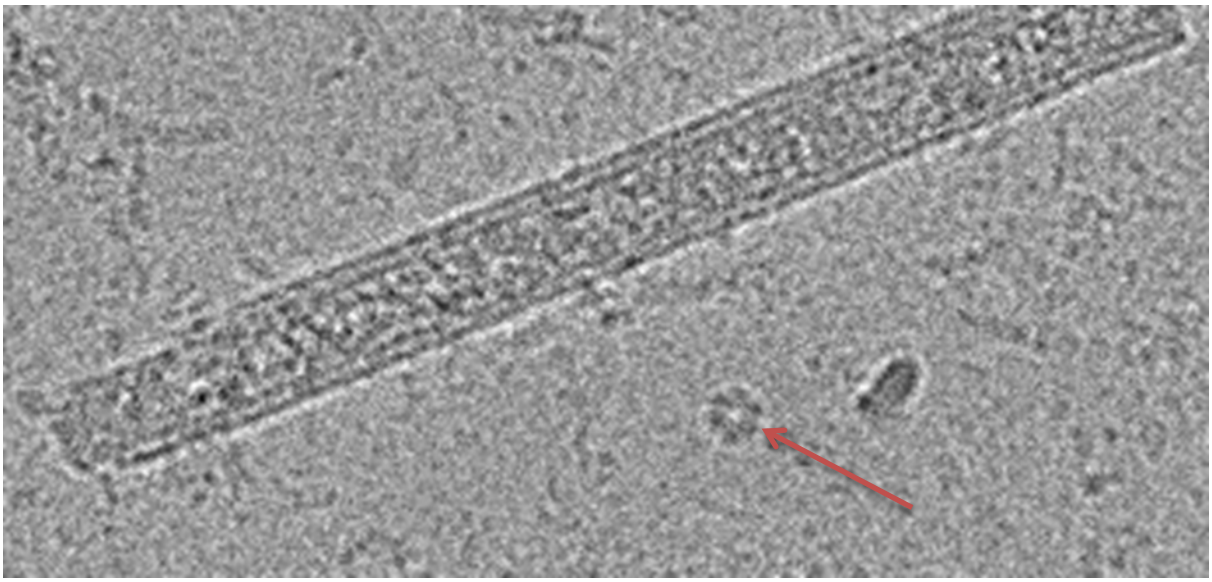

Fig 3.11: Hexameric Spastin Observed Near IST1 Homopolymer. Spastin is monomeric unless bound to ATP and substrate, suggesting that the Spastin hexamer observed here is either

Spastin is thought to only hexamerize when bound to substrate (Eckert et al., 2012), suggesting that this hexamer is either still engaged with substrate, or has very recently disengaged substrate and has not yet disassembled.

Discussion

We have here demonstrated two novel results. First, CHMP1B and IST1 readily polymerize on pulled membrane nanotubes and, in a potentially friction-mediated way, scission them. Second, we have shown that Spastin is capable of disassembling CHMP1B homopolymers and CHMP1B-IST1 heteropolymers in an ATP-independent manner. Both results hint at a physiological role for CHMP1B, IST1, and Spastin in regulating membrane tubes *in vivo* though a polymerization, scission, and recycling process, similar to their reverse-topology kin.

How does Spastin disassemble CHMP1B-IST1 tubes without the need to hydrolyze ATP? A recent high-resolution structure of CHMP1B-IST1 has shown a crucial role for the CHMP1B MIM in stabilizing the heteropolymer by binding to the surface of IST1 (Talledge et al., 2018). The residues on CHMP1B critical for IST1 binding are also critical for binding to Spastin (Talledge et al., 2018; Yang et al., 2008). Therefore, Spastin may disassemble the heteropolymer by binding the CHMP1B MIM and destabilizing the heteropolymer. Given that we observe only IST1 homopolymers after Spastin treatment of heteropolymers, the mechanism may involve Spastin binding the CHMP1B MIM, which causes rearrangement of the polymer and expulsion of CHMP1B, after which the resulting, destabilized IST1 homopolymer spontaneously disassembles, as evidenced by the lack of any polymer after 5 minutes of incubation with Spastin.

It is known that CHMP1B, IST1, and Spastin play a role in the scission of endosomal recycling tubules (Allison et al., 2013). These tubules are responsible for recycling cargo from endosomes to the plasma membrane or golgi, and run parallel to microtubules that carry motor proteins thought to drive tubule growth (Delevoye et al., 2014). It has been demonstrated that IST1 or Spastin knockdown in cells results in persistent survival of endosomal tubules and consequently misregulation of cargo trafficking (Allison et al., 2013). Moreover, both Spastin's microtubule-severing function and its ability to bind ESCRTs are required to properly regulate endosomal tubules function (Allison et al., 2013). F124D Spastin, a mutant unable to bind ESCRTs, is unable to rescue the hyper-tubulation phenotype observed in spastin-knockdown cells (Allison et al., 2013). We therefore suggest that Spastin may play a dual role on endosomal recycling tubes: Spastin binds and disassembles CHMP1B-IST1 heteropolymers, recycling the subunits to the cytosol for further rounds of polymerization while the underlying tubule undergoes scission. Meanwhile, Spastin ensures proper regulation of nearby microtubules through its ATP-dependent microtubule severing activity. Since CHMP1B-IST1 heteropolymer disassembly merely requires Spastin binding in a region distal to its microtubule-binding domain, Spastin may be able to perform both tasks simultaneously.

A major open question with this model is the mechanism of scission. Does Spastin play an active role in the scission process, or does it merely recycle CHMP1B and IST1? Is friction a necessary component to achieve robust scission, in which case motor proteins elongating the tubule may play a major role? And what is the regulation mechanism to prevent Spastin from over-zealously recycling CHMP1B and IST1 before they serve their purpose?

Finally, multiple other functions for this polymer may exist, including the transfer of lipids from peroxisomes to lipid droplets, where Spastin interaction with ESCRT-III controls fatty acid trafficking (Chang et al., 2019), and the scissioning of nascent peroxisomes from the endoplasmic reticulum, where Ist1 deletion results in aberrant peroxisome morphology (Mast et al., 2018). Considering the novelty of this polymer, and considering the explosion of ESCRT functions discovered in recent decades, it is likely that additional physiological roles for this machinery have yet to be discovered.

Materials and Methods

Protein expression, purification, and labelling

CHMP1B and IST1 NTD (AA1-189) were expressed as TEV cleavable, His6-MBP fusion constructs. M87 Spastin was expressed as an N-terminal TEV cleavable His6 fusion construct. CHMP1B and IST1 NTD were transformed into *E. coli* Rosetta2 (DE3) cells, while Spastin was transformed into *E. Coli* BL21 (DE3), and grown to an OD of 0.6 at 37°C, then induced with .5mM IPTG and expressed overnight at 20°C. Cells were harvested by centrifugation, and pellets were lysed in 50mM Tris HCL pH 7.4, 300mM NaCl, 2mM β-mercaptoethanol (βME), sonicated, and clarified by centrifugation. The supernatant was applied to a column containing 5mL bed volume of Ni-NTA resin. After washing with 50mM Tris HCL pH 7.4, 300mM NaCl, 20mM Imidazole buffer, the bound protein was eluted with 50mM Tris HCl pH 7.4, 100mM NaCl, 300mM imidazole. The eluate was applied to a HiLoad 16/60 Superdex s200 chromatography column (GE Healthcare, Chicago, IL, USA) in 50mM Tris pH 7.4, 100mM NaCl, .1mM TCEP. Fractions corresponding to the protein of interest were pooled and their concentration calculated by 280 absorption on a NanoDrop spectrophotometer (Thermo Fischer Scientific, Waltham, MA, USA). CHMP1B and IST1 were labelled by adding 1.2x molar excess

dye (Lumidyne 550, 650, Lumidyne Technologies) to their solutions and incubated either 2h at room temperature, or at 4°C overnight. Following labelling, the proteins were TEV cleaved with TEV protease (.65mg/ml final concentration) for 2 hours at room temperature. Spastin was TEV cleaved immediately after elution from the Ni-NTA column prior to loading on the s200, and the cleaved protein pooled, its concentration measured, and flash frozen in liquid nitrogen. CHMP1B and IST1, after TEV cleaving, were loaded onto a HiLoad 16/60 Superdex s75 (GE Healthcare) chromatography column in 50mM Tris HCl pH 7.4, 300mM NaCl, .1mM TCEP. The purest fractions were determined by SDS-Page and Typhoon scanning for dye absorbance, followed by Coommassie staining. CHMP1B and IST1 concentrations were measured and either flash frozen immediately, or concentrated to 10uM by Amicon Ultra Centrifugal filter (Millipore Sigma), then flash frozen.

GUV preparation

All lipids were obtained from Avanti Polar Lipids (Alabaster, AL). Final lipid mixes were 60% dioleoyl-phosphatidylcholine (DOPC), 40% dioleoyl-phosphatidylserine (DOPS), 0.5 mole% DSPE-PEG(2000)-biotin and 0.5 mole% BODIPY TR ceramide (Avanti Polar Lipids) at 1mg./ml in chloroform. Glass coverslips were coated with a thin film of 5% Poly-vinyl alcohol (PVA) and dried at 50°C for 20 minutes. 15uL of lipid mix was then spread as a thin film across the dried PVA and evaporated under vacuum for at least 1 hour at room temperature. Lipid films were rehydrated at room temperature for 1 hour with GUV swelling buffer (25mM Tris HCl pH 7.4, 70mM NaCl, and glucose to balance the osmolarity of the experimental buffer.)

Microfluidic chamber tube pulling experiments

Adapting a previously used system (Schöneberg et al., 2016), the microfluidic chamber was modified with an additional capillary used to inject protein, in place of a UV-fiber. Injection rate was controlled through the use of a syringe pump (NE-1000 Single Syringe Pump, Pump Systems Inc.) capable of precise, slow flow rates. Flow rate was set to 0.2ul/min, which exerted no detectable force on the membrane nanotube. To inject proteins, the syringe pump was first set to a high flow rate (4ul/s) until proteins filled the chamber. The flow was then halted and the proteins washed out of the chamber. GUVs and beads were then introduced into the chamber. GUVs were aspirated, and optically trapped beads were used to extrude membrane nanotubes. With a tube extruded, the syringe pump was set to 0.2ul/min to inject protein. With various dwell times to due to buffer offsetting protein solution in the capillary, the protein began to arrive at the nanotube and rapidly polymerized on the substrate, after which flow was halted. After a significant amount of protein had polymerized, the bead was first pulled away from the GUV and then pulled back, to induce friction on the nanotube. Scission and retraction to the bead were observed shortly afterward.

Micromanipulator tube pulling experiments

Two instruments were used for tube pulling experiments. The first has been described previously (Sorre et al., 2009). Briefly, a Nikon C1 confocal microscope with dual micromanipulators and optical tweezers and an X60 water immersion objective was used to position micromanipulators. Biotinylated GUVs and streptavidin-coated beads (SVP-30-5, Spherotech) were pipetted into a chamber consisting of two glass coverslips separated by silicon spacers, and allowed to settle. Using one of the micromanipulators, GUVs were aspirated from the coverslip and raised to the

middle of the chamber. Beads were captured using the optical trap and brought into proximity of the GUV. The bead was brought briefly into contact with the GUV to form a streptavidin-biotin interaction, then pulled away, extruding a tube in the process. The second instrument, described previously (Prévost et al., 2015), followed a similar protocol, except a third micromanipulator held the bead instead of an optical trap. In both cases, protein was briefly injected locally onto the tube, after which flow was halted or the micromanipulator moved away, to prevent excessive protein injection. Protein was allowed to polymerize on the tube, after which friction was induced by moving the GUV and bead further apart.

TIRF microtubule disassembly

Microtubule-coated chambers were prepared as described elsewhere (Elshenawy et al., 2020). Briefly, biotinylated microtubules were made by mixing biotin-labelled tubulin with unlabeled pig brain tubulin in BRB80 buffer (80mM PIPES pH 6.8, 1mM $MgCl_2$ and 1mM EGTA), then mixing with polymerization buffer (2x BRB80 buffer with 2mM GTP and 20% DMSO). Tubulin was polymerized for 40 minutes at 37°C, then treated with 10nM taxol, pelleted and resuspended in BRB80 buffer with 1mM DTT. Glass chambers were passivated with BSA and functionalized by flowing a 1mg/ml BSA-Biotin solution, followed by washing with buffer. To immobilize microtubules the chamber was incubated with 1mg/ml streptavidin and washed with buffer. Either buffer or 1uM (final concentration) of Spastin-ATP were added to the chamber while imaging on a custom-built TIRF microscope described in detail elsewhere (Elshenawy et al., 2020).

CHMP1B-IST1 *in vitro* assembly reactions

To assemble CHMP1B and IST1 polymers the proteins were concentrated to 30uM using Amicon Ultra Centrifugal filters (Millipore Sigma). Small unilamellar vesicles consisting of 60% DOPC, 40% DOPS at 2mg/ml final concentration were prepared by drying the lipid mix under nitrogen, resuspending the lipids in 50mM Tris pH 7.4, and sonicating the mixture on ice. The proteins were mixed with the SUVs and dialyzed against 50mM Tris 7.4, 50mM NaCl at room temperature overnight in a Slide-A-Lyzer (ThermoFischer Scientific) cassette. The assembled tubes are harvested the following day. SUVs or IST1 were omitted from the reaction to make CHMP1B-IST1 membrane-less heteropolymers or CHMP1B homopolymers, respectively.

Spastin disassembly experiments

Assembled tubes were gently pelleted for 10 minutes at 3000xg. Supernatant was carefully aspirated and discarded, and the pellet gently resuspended in 50mM Tris HCl pH 7.4, 300mM NaCl. Either buffer or 1uM final concentration Spastin was added, with either ATP/Mg or EDTA. Samples were incubated for 10 minutes, after which they were again pelleted. Supernatant was carefully aspirated and saved, and pellets were resuspended in SDS-PAGE buffer. Supernatants and pellets were run on SDS-PAGE gels, stained with Coommassie, and the band intensity quantitated in ImageJ.

Electron microscopy

For negative-stain experiments, 4uL of tube assembly was applied to glow-discharged continuous carbon-coated copper grids (CF400-CU, Electron Microscopy Sciences) and stained

with 2% w/v uranyl acetate. Grids were imaged on a Tecnai-12 (FEI) operating at 120keV and collected with a CCD (4K TemCam-F416, TVIPS).

For cryo-EM experiments, C-flat 2/1 (Protochips) holey carbon 300 mesh grids were plasma cleaned for 20s at 25mA using a Pelco easiGlow glow discharger (Ted Pella). 3uL of assembled CHMP1B-IST1 polymer solution was applied to the grids, after which either 1uL of Spastin (1uM final) or buffer was added. Samples were incubated for 30 seconds (Spastin) or 5 minutes (buffer, Spastin) before blotting and plunge freezing using a Vitrobot mark VI at 100% humidity and room temperature. Grids were blotted with #1 Whatman paper with blotforce 5 for 3 seconds. Grids were screened on a Talos Arctica operated at 200kV on a K3 direct detector camera.

References

Adell, M. A. Y., Vogel, G. F., Pakdel, M., Müller, M., Lindner, H., Hess, M. W. and Teis, D. (2014). Coordinated binding of Vps4 to ESCRT-III drives membrane neck constriction during MVB vesicle formation. *J. Cell Biol.* **205**, 33–49.

Adell, M. A. Y., Migliano, S. M., Upadhyayula, S., Bykov, Y. S., Sprenger, S., Pakdel, M., Vogel, G. F., Jih, G., Skillern, W., Behrouzi, R., et al. (2017). Recruitment dynamics of ESCRT-III and Vps4 to endosomes and implications for reverse membrane budding. *Elife* **6**, e31652.

Allison, R., Lumb, J. H., Fassier, C., Connell, J. W., Ten Martin, D., Seaman, M. N. J., Hazan, J. and Reid, E. (2013). An ESCRT–spastin interaction promotes fission of recycling tubules from the endosome. *J. Cell Biol.* **202**, 527–543.

Allison, R., Edgar, J. R., Pearson, G., Rizo, T., Newton, T., Günther, S., Berner, F., Hague, J., Connell, J. W., Winkler, J., et al. (2017). Defects in ER–endosome contacts impact lysosome function in hereditary spastic paraplegia. *J. Cell Biol.* **216**, 1337–1355.

Antonny, B., Burd, C., De Camilli, P., Chen, E., Daumke, O., Faelber, K., Ford, M., Frolov, V. A., Frost, A., Hinshaw, J. E., et al. (2016). Membrane fission by dynamin: what we know and what we need to know. *EMBO J.* **35**, 2270–2284.

Babst, M., Wendland, B., Estepa, E. J. and Emr, S. D. (1998). The Vps4p AAA ATPase regulates membrane association of a Vps protein complex required for normal endosome function. *EMBO J.* **17**, 2982–2993.

Babst, M., Katzmann, D. J., Estepa-Sabal, E. J., Meerloo, T. and Emr, S. D. (2002). Escrt-III: An endosome-associated heterooligomeric protein complex required for mvb sorting. *Dev. Cell* **3**, 271–282.

Bajorek, M., Morita, E., Skalicky, J. J., Morham, S. G., Babst, M. and Sundquist, W. I. (2009). Biochemical Analyses of Human IST1 and Its Function in Cytokinesis. *Mol. Biol. Cell* **20**, 1360–1373.

Baumgärtel, V., Ivanchenko, S., Dupont, A., Sergeev, M., Wiseman, P. W., Kräusslich, H.-G., Bräuchle, C., Müller, B. and Lamb, D. C. (2011). Live-cell visualization of dynamics of HIV budding site interactions with an ESCRT component. *Nat. Cell Biol.* **13**, 469–474.

Bertin, A., de Franceschi, N., de la Mora, E., Maity, S., Miguet, N., di Cicco, A., Roos, W., Mangenot, S., Weissenhorn, W. and Bassereau, P. (2019). Human ESCRT-III Polymers Assemble on Positively Curved Membranes and Induce Helical Membrane Tube Formation. *bioRxiv* 847319.

Bleck, M., Itano, M. S., Johnson, D. S., Thomas, V. K., North, A. J., Bieniasz, P. D. and Simon, S. M. (2014). Temporal and spatial organization of ESCRT protein recruitment during HIV-1 budding. *Proc. Natl. Acad. Sci.* **111**, 12211–12216.

Campsteijn, C., Vietri, M. and Stenmark, H. (2016). Novel ESCRT functions in cell biology: spiraling out of control? *Curr. Opin. Cell Biol.* **41**, 1–8.

Carlson, L.-A., Shen, Q.-T., Pavlin, M. R. and Hurley, J. H. (2015). ESCRT Filaments as Spiral Springs. *Dev. Cell* **35**, 397–398.

Cashikar, A. G., Shim, S., Roth, R., Maldazys, M. R., Heuser, J. E. and Hanson, P. I. (2014). Structure of cellular ESCRT-III spirals and their relationship to HIV budding. *Elife* **3**,.

Chang, C.-L., Weigel, A. V, Ioannou, M. S., Pasolli, H. A., Xu, C. S., Peale, D. R., Shtengel, G., Freeman, M., Hess, H. F., Blackstone, C., et al. (2019). Spastin tethers lipid droplets to peroxisomes and directs fatty acid trafficking through ESCRT-III. *J. Cell Biol.* **218**, 2583–2599.

Chiaruttini, N. and Roux, A. (2017). Dynamic and elastic shape transitions in curved ESCRT-III filaments. *Curr. Opin. Cell Biol.* **47**, 126–135.

Chiaruttini, N., Redondo-Morata, L., Colom, A., Humbert, F., Lenz, M., Scheuring, S. and Roux, A. (2015). Relaxation of Loaded ESCRT-III Spiral Springs Drives Membrane Deformation. *Cell* **163**, 866–879.

De Franceschi, N., Alqabandi, M., Miguet, N., Caillat, C., Mangenot, S., Weissenhorn, W. and Bassereau, P. (2019). The ESCRT protein CHMP2B acts as a diffusion barrier on reconstituted membrane necks. *J. Cell Sci.* **132**, jcs217968.

Delevoye, C., Miserey-Lenkei, S., Montagnac, G., Gilles-Marsens, F., Paul-Gilloteaux, P., Giordano, F., Waharte, F., Marks, M. S., Goud, B. and Raposo, G. (2014). Recycling Endosome Tubule Morphogenesis from Sorting Endosomes Requires the Kinesin Motor KIF13A. *Cell Rep.* **6**, 445–454.

Derényi, I., Jülicher, F. and Prost, J. (2002). Formation and Interaction of Membrane Tubes. *Phys. Rev. Lett.* **88**, 238101.

Dobro, M. J., Samson, R. Y., Yu, Z., McCullough, J., Ding, H. J., Chong, P. L.-G., Bell, S. D. and Jensen, G. J. (2013). Electron cryotomography of ESCRT assemblies and dividing Sulfolobus cells suggests that spiraling filaments are involved in membrane scission. *Mol. Biol. Cell* **24**, 2319–2327.

Eckert, T., Link, S., Le, D. T.-V., Sobczak, J.-P., Gieseke, A., Richter, K. and Woehlke, G. (2012). Subunit Interactions and Cooperativity in the Microtubule-severing AAA ATPase Spastin. *J. Biol. Chem.* **287**, 26278–26290.

Elia, N., Sougrat, R., Spurlin, T. A., Hurley, J. H. and Lippincott-Schwartz, J. (2011). Dynamics of endosomal sorting complex required for transport (ESCRT) machinery during cytokinesis and its role in abscission. *Proc. Natl. Acad. Sci.* **108**, 4846–4851.

Elia, N., Fabrikant, G., Kozlov, M. M. and Lippincott-Schwartz, J. (2012). Computational Model of Cytokinetic Abscission Driven by ESCRT-III Polymerization and Remodeling. *Biophys. J.* **102**, 2309–2320.

Elshenawy, M. M., Kusakci, E., Volz, S., Baumbach, J., Bullock, S. L. and Yildiz, A. (2020). Lis1 activates dynein motility by modulating its pairing with dynactin. *Nat. Cell Biol.* **22**, 570–578.

Guizetti, J., Schermelleh, L., Mäntler, J., Maar, S., Poser, I., Leonhardt, H., Müller-Reichert, T. and Gerlich, D. W. (2011). Cortical Constriction During Abscission Involves Helices of ESCRT-III–Dependent Filaments. *Science* **331**, 1616–1620.

Hanson, P. I. and Cashikar, A. (2012). Multivesicular Body Morphogenesis. *Annu. Rev. Cell Dev. Biol.* **28**, 337–362.

Hanson, P. I., Roth, R., Lin, Y. and Heuser, J. E. (2008). Plasma membrane deformation by circular arrays of ESCRT-III protein filaments. *J. Cell Biol.* **180**, 389–402.

Henne, W. M., Stenmark, H. and Emr, S. D. (2013). Molecular Mechanisms of the Membrane Sculpting ESCRT Pathway. *Cold Spring Harb. Perspect. Biol.* **5**,.

Hurley, J. H. and Yang, D. (2008). MIT Domainia. *Dev. Cell* **14**, 6–8.

Johnson, D. S., Bleck, M. and Simon, S. M. (2018). Timing of ESCRT-III protein recruitment and membrane scission during HIV-1 assembly. *Elife* **7**, e36221.

Jouvenet, N., Zhadina, M., Bieniasz, P. D. and Simon, S. M. (2011). Dynamics of ESCRT protein recruitment during retroviral assembly. *Nat. Cell Biol.* **13**, 394–401.

Lata, S., Schoehn, G., Jain, A., Pires, R., Piehler, J., Gőttlinger, H. G. and Weissenhorn, W. (2008). Helical Structures of ESCRT-III Are Disassembled by VPS4. *Science* **321**, 1354–1357.

Lenz, M., Crow, D. J. G. and Joanny, J.-François (2009). Membrane Buckling Induced by Curved Filaments. *Phys. Rev. Lett.* **103**, 38101.

Mast, F. D., Herricks, T., Strehler, K. M., Miller, L. R., Saleem, R. A., Rachubinski, R. A. and Aitchison, J. D. (2018). ESCRT-III is required for scissioning new peroxisomes from the endoplasmic reticulum. *J. Cell Biol.* **217**, 2087–2102.

McCullough, J., Colf, L. A. and Sundquist, W. I. (2013). Membrane Fission Reactions of the Mammalian ESCRT Pathway. *Annu. Rev. Biochem.* **82**, 663–692.

McCullough, J., Clippinger, A. K., Talledge, N., Skowyra, M. L., Saunders, M. G., Naismith, T. V., Colf, L. A., Afonine, P., Arthur, C., Sundquist, W. I., et al. (2015a). Structure and membrane remodeling activity of ESCRT-III helical polymers. *Sci.* **350**, 1548–1551.

McCullough, J., Clippinger, A. K., Talledge, N., Skowyra, M. L., Saunders, M. G., Naismith, T. V., Colf, L. A., Afonine, P., Arthur, C., Sundquist, W. I., et al. (2015b). Structure and membrane remodeling activity of ESCRT-III helical polymers. *Science* **350**, 1548–1551.

Mierzwa, B. E., Chiaruttini, N., Redondo-Morata, L., Moser von Filseck, J., König, J., Larios, J., Poser, I., Müller-Reichert, T., Scheuring, S., Roux, A., et al. (2017). Dynamic subunit turnover in ESCRT-III assemblies is regulated by Vps4 to mediate membrane remodelling during cytokinesis. *Nat. Cell Biol.* **19**, 787.

Nguyen, H. C., Talledge, N., McCullough, J., Sharma, A., Moss, F. R., Iwasa, J. H., Vershinin, M. D., Sundquist, W. I. and Frost, A. (2020). Membrane constriction and thinning by sequential ESCRT-III polymerization. *Nat. Struct. Mol. Biol.* **27**, 392–399.

Obita, T., Saksena, S., Ghazi-Tabatabai, S., Gill, D. J., Perisic, O., Emr, S. D. and Williams, R. L. (2007). Structural basis for selective recognition of ESCRT-III by the AAA ATPase Vps4. *Nature* **449**, 735–739.

Olmos, Y. and Carlton, J. G. (2016). The ESCRT machinery: new roles at new holes. *Curr. Opin. Cell Biol.* **38**, 1–11.

Pfitzner, A.-K., Mercier, V. and Roux, A. (2019). Vps4 triggers sequential subunit exchange in ESCRT-III polymers that drives membrane constriction and fission. *bioRxiv* 718080.

Prévost, C., Zhao, H., Manzi, J., Lemichez, E., Lappalainen, P., Callan-Jones, A. and Bassereau, P. (2015). IRSp53 senses negative membrane curvature and phase separates along membrane tubules. *Nat. Commun.* **6**, 8529.

Roll-Mecak, A. and Vale, R. D. (2008). Structural basis of microtubule severing by the hereditary spastic paraplegia protein spastin. *Nature* **451**, 363–367.

Schöneberg, J., Lee, I.-H., Iwasa, J. H. and Hurley, J. H. (2016). Reverse-topology membrane scission by the ESCRT proteins. *Nat. Rev. Mol. Cell Biol.* **18**, 5.

Schöneberg, J., Pavlin, M. R., Yan, S., Righini, M., Lee, I.-H., Carlson, L.-A., Bahrami, A. H., Goldman, D. H., Ren, X., Hummer, G., et al. (2018). ATP-dependent force generation and membrane scission by ESCRT-III and Vps4. *Science* **362**, 1423–1428.

Shen, Q.-T., Schuh, a. L., Zheng, Y., Quinney, K., Wang, L., Hanna, M., Mitchell, J. C., Otegui, M. S., Ahlquist, P., Cui, Q., et al. (2014). Structural analysis and modeling reveals new mechanisms governing ESCRT-III spiral filament assembly. *J. Cell Biol.* **206**, 763–777.

Shnyrova, A. V, Bashkirov, P. V, Akimov, S. A., Pucadyil, T. J., Zimmerberg, J., Schmid, S. L. and Frolov, V. A. (2013). Geometric Catalysis of Membrane Fission Driven by Flexible Dynamin Rings. *Science* **339**, 1433–1436.

Simunovic, M., Manneville, J.-B., Renard, H.-F., Evergren, E., Raghunathan, K., Bhatia, D., Kenworthy, A. K., Voth, G. A., Prost, J., McMahon, H. T., et al. (2017). Friction Mediates Scission of Tubular Membranes Scaffolded by BAR Proteins. *Cell* **170**, 172-184.e11.

Sorre, B., Callan-Jones, A., Manneville, J.-B., Nassoy, P., Joanny, J.-F., Prost, J., Goud, B. and Bassereau, P. (2009). Curvature-driven lipid sorting needs proximity to a demixing point and is aided by proteins. *Proc. Natl. Acad. Sci.* **106**, 5622–5626.

Stuchell-Brereton, M. D., Skalicky, J. J., Kieffer, C., Karren, M. A., Ghaffarian, S. and Sundquist, W. I. (2007). ESCRT-III recognition by VPS4 ATPases. *Nature* **449**, 740–744.

Talledge, N., McCullough, J., Wenzel, D., Nguyen, H. C., Lalonde, M. S., Bajorek, M., Skalicky, J., Frost, A. and Sundqust, W. I. (2018). The ESCRT-III proteins IST1 and CHMP1B assemble around nucleic acids. *bioRxiv* 386532.

Teis, D., Saksena, S. and Emr, S. D. (2008). Ordered Assembly of the ESCRT-III Complex on Endosomes Is Required to Sequester Cargo during MVB Formation. *Dev. Cell* **15**, 578–589.

Vietri, M., Schink, K. O., Campsteijn, C., Wegner, C. S., Schultz, S. W., Christ, L., Thoresen, S. B., Brech, A., Raiborg, C. and Stenmark, H. (2015). Spastin and ESCRT-III coordinate mitotic spindle disassembly and nuclear envelope sealing. *Nature* **522,** 231-235

von Filseck, J. M., Barberi, L., Talledge, N., Johnson, I., Frost, A., Lenz, M. and Roux, A. (2019). Anisotropic ESCRT-III architecture governs helical membrane tube formation. *bioRxiv* 716308.

Wollert, T. and Hurley, J. H. (2010). Molecular mechanism of multivesicular body biogenesis by ESCRT complexes. *Nature* **464**, 864–869.

Wollert, T., Wunder, C., Lippincott-Schwartz, J. and Hurley, J. H. (2009). Membrane scission by the ESCRT-III complex. *Nature* **458**, 172–177.

Yang, D., Rismanchi, N., Renvoisé, B., Lippincott-Schwartz, J., Blackstone, C. and Hurley, J. H. (2008). Structural basis for midbody targeting of spastin by the ESCRT-III protein CHMP1B. *Nat. Struct. Mol. Biol.* **15**, 1278–1286.

Zamborlini, A., Usami, Y., Radoshitzky, S. R., Popova, E., Palu, G. and Göttlinger, H. (2006). Release of autoinhibition converts ESCRT-III components into potent inhibitors of HIV-1 budding. *Proc. Natl. Acad. Sci.* **103**, 19140–19145.

Acknowledgements: We thanks Feng-Ching Tsai, Nicola De Franceschi, and the Bassereau lab for inviting us to perform tube pulling experiments in their lab, and their assistance with the experiments. We thank Luke Ferro for assistance performing TIRF microtubule disassembly assays.

Chapter 4

Conclusions and Perspective

The ESCRTs are a fascinating, highly complex machinery. We have here shown both a major advance in understanding one of the functions of the ESCRTs, in chapter 2, and then revealed a novel mechanism that raises yet more questions in chapter 3. While the past decade has yielded massive gains in our understanding of ESCRT function, it has also revealed many gaps in our knowledge.

We now know that the ESCRTs truly are everywhere. From their well-studied function in Multi-Vesicular Body Biogenesis to their esoteric function in pyroptosis, the ESCRTs present a daunting cell-biological challenge. It will be essential, in understanding this machinery, to create a thorough database of their physiological functions: the biological process, the adaptors that recruit the ESCRTs, the specific ESCRTs involved, the geometry of assembly, the topology of scission, the timescales involved, and the other factors, such as AAA+ ATPases, involved. The field is rich with processes to study, with even more ESCRT functions likely yet to be discovered.

Mechanistically the ESCRTs provide a similarly daunting challenge. A highly dynamic machinery with dozens of components rapidly rearranging themselves presents immense difficulty to mechanistic study. Despite this, much progress has been made in recent years, in part by bringing new technologies into the field. In addition to the tube pulling experiments described in detail in chapters 1 and 2, cryo-electron tomography will becoming increasingly critical to understanding the ESCRTs. With clever sample design a snapshot of the ESCRT machinery could be imaged with this technique, revealing structural intermediates in the process that have long been central to the question of mechanism.

Finally, an interesting question is whether a single mechanism can even explain ESCRT function, or whether the machinery has evolved multiple distinct mechanisms for specific pathways. Cytokinesis has long been an outlier for reverse-topology membrane scission due to the large time and length scales involved. Recent findings, however, suggest entirely distinct mechanisms. Normal topology scission by CHMP1B and IST1 suggest that at least some of the ESCRTs do not function exclusively in reverse-topology processes. Observations that "canonical" reverse-topology subunits such as Snf7, Vps2, and Vps24 deform membranes into helical tubes, and are involved in the scission of nascent peroxisomes from the ER, hint that the ESCRTs are more broadly a membrane remodeling machinery not tied to reverse-topology functions.

While much progress has been made, many crucial questions remain. With new technologies and clever experiments, we can look forward to exciting new developments to finally understand this wonderful, mysterious machinery.